

Why, how and when electrically driven flows and MHD turbulence become *three*-dimensional

A. Pothérat¹ and R. Klein²

¹Applied Mathematics Research Centre,
Coventry University, Coventry CV5 8HY, UK

²Technische Universität Ilmenau, Fakultät für Maschinenbau,
Postfach 100565, 98684 Ilmenau Germany

May 30th, 2013

Abstract

The dimensionality of electrically driven flows and magnetohydrodynamic (MHD) turbulence at low Magnetic Reynolds number is analysed by driving a square array of vortices of alternate spin in a cubic vessel filled with liquid metal, placed in a high homogeneous, static magnetic field \mathbf{B} . A wide range of steady and unsteady flows is generated by varying the intensity I of the DC current injected to drive them, and their dimensionality is influenced by increasing or decreasing the magnetic field intensity.

After a review of the flow regimes attained from a steady array of columnar vortices aligned with the magnetic field, to three-dimensional turbulence, it is shown theoretically, and then experimentally that three-dimensionality is characterised by scaling laws linking the core velocity U_b near the wall where current is injected to the current intensity I , of either forms $U_b \sim I$ or $U_b \sim I^{2/3}$, depending on whether three-dimensionality originates from viscous or inertial effects. In turbulent flows. The opposite wall is found to be either active or passive depending whether the ratio of its distance to the bottom wall h to the length $l_z \sim N_t^{1/2}$, over which the Lorentz force diffuses momentum along \mathbf{B} is larger or smaller than unity (where N_t is the "true" interaction parameter introduced by Sreenivasan & Albuossière (2002)). The diffusive nature of the Lorentz force at low magnetic Reynolds number, first theorised by Sommeria & Moreau (1982), is thus observed and quantified for the first time. It also turns out that when $l_z < h$, turbulent fluctuations bear little trace of the three-dimensional nature of the forcing. Finally, weak and strong three-dimensionalities, which respectively involve variations along \mathbf{B} in flow intensity only, and variations both of flow intensity and topology, were separately quantified. Both were found to vanish only asymptotically in the limit $N_t \rightarrow \infty$. This provides evidence that because of the no-slip walls, the 2D-3D transition does not result from a global instability of the flow, unlike in domains with non-dissipative boundaries (Thess & Zikanov (2007)). It is further shown that strong three-dimensionality is sharply scale-selective and that it does only affect structures of a size below a cutoff value, as theorised by Sommeria & Moreau (1982).

Keywords: low Rm Magnetohydrodynamics, turbulence dimensionality, vortex dynamics, two-dimensional turbulence.

1 Introduction

This paper presents an attempt to inventorise the mechanisms that determine the dimensionality of electrically driven flows and magnetohydrodynamic (MHD) turbulence. The approach consists

of experimentally probing a large variety of flow regimes obtained by driving a square array of vortices in a liquid metal exposed to a high magnetic field.

The questions of characterising and determining flow dimensionality are ones of interest well beyond the field of liquid metal MHD. The excitement around them possibly stems from the spectacular difference between the respective dynamics of two- and three-dimensional turbulence. While the former is most often associated with the process of inverse energy cascade, in which energy is transferred from smaller to larger scales (see Kraichman (1967, 1971), and Tabeling (2002); Clercx & Van Heijst (2009) for recent reviews), the latter most often displays the opposite phenomenon: a direct energy cascade, where energy is passed on to smaller and smaller scales until it is dissipated by viscous friction at the *Kolmogorov scale* (Kolmogorov (1941)). While in two-dimensional turbulence, large scale transport is prominent and dissipation mostly occurs through friction at the boundaries of the domain, small-scale mixing and dissipation in three-dimensional turbulence are intense everywhere in the bulk of the flow. The question of whether flows obey two or three-dimensional dynamics in this sense is, however, not trivially related to flow dimensionality: flows can be two dimensional (2D) in the sense that velocity and pressure do not vary in one dimension of space but still possess three non-zero velocity components (such flows are sometimes referred to as 2D-3C). Toschi *et al.* (2012) even showed recently that an inverse energy cascade could also be found in homogeneous 3D turbulence.

From the practical point of view, whether turbulence obeys two or three-dimensional dynamics has drastic consequences for the natural and industrial processes where it is involved, and this concern numerous classes of realistic systems: the tendency to two-dimensionality in stratified flows (Paret J. & P. (1997)) and rotating flows (Greenspan (1969)) is a prominent feature of planetary flows such as atmospheres and oceans, and the dynamics of large atmospheric vortices is, to some extent, two-dimensional. Electrically conducting flows under a strong magnetic field exhibit this remarkable feature too, which extends the relevance of the question of flow dimensionality to astrophysical flows and plasmas, but also to engineering problems where liquid metals are exposed to magnetic fields. These range from the optimisation of heat and mass exchangers such as the liquid metal blankets, designed to harvest the large amount of heat generated by nuclear fusion in tokamaks, to the electromagnetic control of steel casting or of silicone crystal growth for semi-conductor applications. This common tendency to two-dimensionality nevertheless hides a variety of physical mechanisms: while the propagation of gravity waves across density gradients and of inertial waves along the rotation promote two-dimensionality in stratified and rotating flows respectively, eddy currents induced by gradients of velocity across magnetic field lines play this role in MHD flows. If advection of magnetic field by the flow cannot be neglected compared to the magnetic field diffusion time, these generate Alfvén waves, which propagate along them (Roberts (1967)). Otherwise, if the ratio of these effects, measured by the magnetic Reynolds number Rm , is very small, the Lorentz force associated to these currents acts so as to diffuse momentum along \mathbf{B} in a time scale of $\tau_{2D}(l_{\perp}, l_z) = \rho/(\sigma B^2)(l_z/l_{\perp})^2$, where l_z and l_{\perp} are the lengthscale of the considered flow structure, respectively along and across the imposed magnetic field \mathbf{B} (Sommeria & Moreau (1982)). It is this later case, which this paper is concerned with.

Historically, it was the tendency to two-dimensionality, and the associated growth of anisotropy that was first investigated, rather than the question of transition between two and three-dimensionality. Moffatt (1967), first recognised 2D-3C flows as the asymptotic state of decaying turbulence under an externally imposed magnetic field at low Rm , while Shebalin *et al.* (1983) observed the growth of anisotropy at high Rm too in plasmas where a strong mean magnetic field was present. At low Rm , Numerical simulations of forced MHD turbulence in a domain bounded by periodic boundary conditions later showed the first evidence of two-dimensional MHD flows, in conditions where the interaction parameter $N = \tau_u/\tau_J$ which expresses the ratio of the turnover time of the large scales τ_u to the Joule time $\tau_J = \rho/(\sigma B^2)$ (which characterises electromagnetic dissipation) was

significantly larger than unity (Schumann (1976); Zikanov & Thess (1998)). Boeck *et al.* (2008) found, still numerically, that at moderate interaction parameters, a dynamical instability could lead the flow to shift intermittently between two and three-dimensional states, a phenomenon that Thess & Zikanov (2007) also found in ellipsoidal domains with slip-free boundaries while Pothérat & Dymkou (2010) showed that for a flow in a given magnetic field, three-dimensionality appeared at a bifurcation when the intensity of a 2D-2C flow intensity was increased. All these studies with dissipation-free boundaries drew a picture where three-dimensionality developed as an instability on initially two-dimensional (and two component) flows.

Experiments, by contrast, never feature entirely slip-free boundaries. For this reason at least, the picture which experimentalists were facing was in fact very different. The first major attempt to understand the conditions in which MHD flows become two-dimensional with realistic boundaries was, paradoxically, theoretical. In a seminal paper to which the title of this work pays tribute, Sommeria & Moreau (1982) first noted that because of the *Hartmann boundary layers* that develop along the walls bounding a fluid layer orthogonal to an external magnetic field, the flow could be at best quasi-two dimensional and not strictly two-dimensional (see Moreau (1990) for a complete theory of these layers). Nevertheless, in the limit $Ha \rightarrow \infty$ and $N \rightarrow \infty$, where the squared Hartmann number Ha^2 measures the ratio of Lorentz to viscous forces, the dynamics of quasi-two dimensional flows only differs from that of two-dimensional flows through an added linear friction due to these layers. Sommeria (1986) later went on to give an experimental evidence of an inverse energy cascade in this configuration. Yet, Sommeria & Moreau (1982)'s theory doesn't exclude that three-dimensionality may appear as an instability in quasi-two dimensional flows. In fact, they suggested that structures of lengthscale l_{\perp} across \mathbf{B} could be disrupted by inertial effects if their turnover time was shorted than the typical time for the electromagnetic diffusion of their momentum across the channel (of width h), $\tau_{2D}(l_{\perp}, h)$. This led them to derive a cutoff scale $l_{\perp}^c \sim N^{1/3}$, above which structures would be quasi-two dimensional and below which they would be three-dimensional.

On the top of this phenomenology, actual experiments suggest that no-slip boundaries and the nature of the forcing bring general mechanisms not specific to MHD in play: in the absence of magnetic field, Akkermans *et al.* (2008) found that the transversal velocity component almost always subsisted in thin layers of fluid, whether these rested on a no-slip surface or a buffer-layer of fluid, which reduced but didn't completely suppress boundary friction. MHD experiments on thin layers of liquid metal confined between two parallel walls showed similar phenomena, with secondary flows akin to Ekman pumping capable of strongly modifying the quasi-two dimensional dynamics of the flow (Alboussière *et al.* (1999); Pothérat *et al.* (2000, 2005)). Asymptotic analysis showed that these secondary flows also induced three-dimensionality, with a quadratic variation of velocity across the fluid layer called *Barrel effect*. In MHD flows, a formally analogous mechanisms led to three-dimensionality induced by eddy current recirculating between the Hartmann layers and the bulk of the flow, (Pothérat (2012); Pothérat *et al.* (2000); Mück *et al.* (2000)). Conversely, an inhomogeneous forcing across the fluid layer non only drives three-dimensionality in the flow, but the resulting three-dimensional structures were recently found to induce secondary flows with a transverse velocity component which overrides Ekman pumping (Pothérat *et al.* (2013)). These results concur to show that whether induced by the boundaries or by the inhomogeneity of the forcing, the appearance of three-dimensionality and that of the third component are inter-dependent, and also that they do not always result from instabilities in quasi-two dimensional flows.

Clearly, in all applications of interest walls are present and flow forcing is never perfectly two-dimensional itself, so most of the mechanisms discussed above potentially act simultaneously. This makes the challenge of understanding the transition between two and three-dimensional states significantly more difficult than in idealised situations, but also all the more necessary to unveil a realistic picture. It is this task which shall be undertaken in this paper. Our approach con-

sists of forcing turbulence between two Hartmann walls (*i.e.* orthogonal to an externally imposed magnetic field) by injecting a DC current driving square arrays of vortices of alternate spin, as Sommeria (1986) did. It relies on a precise flow mapping based on the simultaneous non-intrusive measurement of the time-dependent electric potential at the wall of vessel. We shall pursue four main objectives:

1. characterise the mechanisms driving a progressive appearance of three-dimensionality, and quantify them,
2. clarify the role of the bounding walls in the appearance of three-dimensionality,
3. characterise three-dimensionality induced by instabilities and experimentally verify Sommeria & Moreau (1982)'s theoretical prediction of the existence of a cutoff structure size separating quasi-two and three dimensional structures.
4. distinguish mechanisms linked by the three-dimensionality of the forcing from those intrinsic to the flow dynamics.

The layout of this paper is as follows. Since our experiment is based on non-intrusive measurements of electric potentials at the walls defining the fluid domain, we first establish theoretical scalings linking near-wall velocities to the intensity of the electric current, which is injected to drive the flow. This is done in the canonical case of an isolated vortex confined between two Hartmann walls. Several different such scalings are obtained, depending on whether the flow is quasi-two dimensional or three-dimensional and whether three-dimensionality is driven by inertia or viscous forces (section 2). Once armed with this theoretical instrument to diagnose flow dimensionality out of measurements at the walls, we proceed to describe the experimental platform FLOWCUBE, which allows us to produce a variety of flows ranging to a square array of steady vortices in a cubic vessel to full-blown three-dimensional turbulence (section 3). Before analysing flow dimensionality, we first map the complex landscape of flow regimes spanned with FLOWCUBE in the space of control parameters (section 4). We then navigate this map to determine all possible occurrences of three-dimensionality in the light of the scalings derived in section 2 (section 5). This global picture of the flow dimensionality is finally refined by means of frequency by frequency analysis, in which we distinguish weak and strong three-dimensionality, (first introduced in Klein & Pothérat (2010)) (section 6).

2 Basic theory

2.1 Governing equations and governing parameters

In the low- Rm approximation (Roberts (1967)), the motion of an electrically conducting fluid (electric conductivity σ , density ρ and kinematic viscosity ν) in an ambient magnetic field \mathbf{B} induces an electric current density \mathbf{J} . In turn, their mutual interaction creates a Lorentz force density $\mathbf{J} \times \mathbf{B}$ on the flow, which drives the physical mechanisms which this paper is devoted to. The magnetic field associated to the induced current is of the order of $\mu\sigma ULB = RmB$. Since, in the experimental configuration considered here, the magnetic Reynolds number Rm remains well below 10^{-1} , the flow-induced component of the magnetic field can be safely neglected and \mathbf{B} shall coincide with the externally imposed field $B\mathbf{e}_z$. In these conditions, mechanical and electromagnetic quantities are only coupled through the mutual dependence of the velocity and pressure fields \mathbf{u} and p , on one side and the electric current density \mathbf{J} on the other. The governing equations consist of the Navier-Stokes equations

$$\partial_t \mathbf{u} + \mathbf{u} \cdot \nabla \mathbf{u} + \frac{1}{\rho} \nabla p = \nu \nabla^2 \mathbf{u} + B \mathbf{J} \times \mathbf{e}_z, \quad (1)$$

Ohm's law

$$\frac{1}{\sigma} \mathbf{J} = -\nabla\phi + B\mathbf{u} \times \mathbf{e}_z, \quad (2)$$

where ϕ is the electric potential, and the equations expressing the conservation of mass and charge, respectively:

$$\nabla \cdot \mathbf{u} = 0, \quad (3)$$

$$\nabla \cdot \mathbf{J} = 0. \quad (4)$$

With a choice of reference velocity U , reference lengths across and along the magnetic field l_\perp and l_z , time, pressure, electric current density and electric potential can respectively be normalised by l_\perp/U , ρU^2 , $\sigma B U$ and $B U L$ and it turns out that the system (1-4) is determined by three non-dimensional parameters:

$$Ha = B l_z \sqrt{\frac{\sigma}{\rho \nu}}, \quad N = \frac{\sigma B^2 l_\perp}{\rho U}, \quad \lambda = \frac{l_\perp}{l_z}. \quad (5)$$

Ha^2 expresses the ratio of Lorentz to viscous forces, while the interaction parameter N is a coarse estimate of the ratio of Lorentz to inertial forces and λ is the aspect ratio of the considered fluid structure. The effect of the Lorentz force at low Rm comes into light through the curl of Ohm's law (2), and by virtue of (3):

$$\nabla \times \mathbf{J} = \sigma B \partial_z \mathbf{u}. \quad (6)$$

(6) expresses that gradients of velocity along \mathbf{B} are necessary to induce electric currents. (6) and charge conservation impose that these must form eddy currents of intensity proportional to the local velocity difference, and which tend to loop back where velocity is lowest. The associated Lorentz force density tends to dampen the velocity gradient. In the absence of a free surface, only its rotational part shall affect the flow, which, by virtue of (6) can be expressed through:

$$\nabla^2 \mathbf{F}_l = -\sigma B^2 \partial_{zz}^2 \mathbf{u} - \nabla(\sigma B^2 \partial_z u_z). \quad (7)$$

In configurations where boundary conditions guarantee the existence of the inverse laplacian Δ^{-1} , Sommeria & Moreau (1982) deduced from this expression that, at low Rm , the Lorentz force diffuses momentum in the direction of the magnetic field over a distance l_z , in characteristic time $\tau_{2D}(l_z) = \tau_J \lambda^{-2}$. Interestingly, this mechanism does not involve the momentum equation (1) and thus remains valid regardless of the incompressible fluid considered. Based on this more precise phenomenology, Sreenivasan & Alboussière (2002) defined a *true* interaction parameter $N_t = N \lambda^{-2}$, which represents the ratio of the diffusive effect of the Lorentz force to inertial effects more accurately than N .

Conversely, in the limit $N_t \rightarrow \infty$, $Ha \rightarrow \infty$, The Lorentz force dominates all others and, boundary conditions permit, the flow can become strictly two-dimensional. Eddy currents then vanish and so does the Lorentz force. A through current J_z can still be non-zero, but does not interact with the flow.

2.2 Quasi-two dimensional electrically driven flows

The canonical configuration which our experiment targets is that of flows bounded by two electrically insulating walls orthogonal to \mathbf{B} , located at $z = 0$ and $z = h$. It is then natural to replace l_z with h in the definition of all three non-dimensional parameters (5). In this case, the no-slip boundary condition at the wall imposes that viscous friction must oppose \mathbf{F}_L in the Hartmann boundary layers near the wall. The balance between these effects determines the thickness of these

layers as $\delta_H = h/Ha$ and in the absence of inertia, their laminar profile is a simple exponential function of the distance to the wall (see for instance Moreau (1990) for the full theory of these layers).

The flow is driven by injecting electric current at point electrodes embedded in the otherwise electrically insulating bottom wall. Let us consider one such electrode where a current I enters the flow. In the limit $Ha \rightarrow \infty$ and $N \rightarrow \infty$, $\nabla \times (1)$ implies that $\nabla_{\perp} \cdot \mathbf{J}_{\perp} = 0$, so the current cannot flow radially in the core. It must therefore either pass through the Hartmann layers, or continue to flow vertically from the electrode where it is injected into the flow. If U_b is the azimuthal velocity in the core at $(r, z = \delta_H)$ in cylindrical coordinates associated with the electrode, (*i.e.* just outside the Hartmann the layer), then noting that $J_z \simeq 0$ away from the electrode, (6) yields an estimate for the total outward current: $I_b \sim 2\pi U_b \sqrt{\rho\sigma\nu}^{1/2}$, where I_b is the fraction of I that passes through the Hartmann layer. Since current conservation makes it valid at all r , the vortex profile near the bottom walls is:

$$U_b(r) \simeq \frac{I_b}{2\pi r \sqrt{\rho\sigma\nu}^{1/2}}. \quad (8)$$

In the absence of any upper boundary, and without any viscous or inertial forces in the core, $\partial_z u_{\theta}(z) = 0$ so an infinitely high column of fluid would be set in motion at velocity $U_b(r)$ by injecting a finite amount of current. Unfortunately, this apparent paradox simply implies that $I_b = 0$. If, on the other hand, a stress-free boundary exists at $z = h$, then since no Hartmann boundary layer develops along it, the current $I - I_b$ injected vertically into the core must turn back along the viscous vortex core and enter the bottom Hartmann layer near the electrode. Thus, $I = I_b$, and this geometry with a single Hartmann layer recovers that studied by Sommeria (1988). Expression (8) precisely matches that rigorously derived by Sommeria (1988) for his experiment on electrically driven flows bounded by an upper free surface.

In the case of a channel as studied in this paper, quasi-two dimensionality in the core implies that a second boundary layer, exactly symmetric to the bottom one, is present near the top wall. Such a configuration, with two axisymmetric vortices, is represented in figure 1 (c). The radial current $I_t = I_b$ in the top layer must therefore be fed by a vertical current in the centre of the vortex, above the electrode and so $I_t = I_b = I/2$: U_b is half of the value found when a free surface is present.

2.3 Three-dimensional electrically driven axisymmetric vortex

We now turn our attention to cases where either Ha or N is finite. From the curl of (1), finite viscous or inertial effects drive a divergent current in the core:

$$\partial_z J_z = -\nabla_{\perp} \cdot \mathbf{J}_{\perp} = \frac{\rho}{B} (\mathbf{u} \cdot \nabla \omega_z + \omega \cdot \nabla \mathbf{u}) - \frac{\rho\nu}{B} \nabla^2 \omega_z. \quad (9)$$

Let us first consider an axisymmetric vortex materialised by a purely azimuthal velocity field $\mathbf{u} = u_{\theta}(r, z)\mathbf{e}_{\theta}$. Inertial terms are then exactly 0, and (9) expresses that viscous forces in the core are balanced by an azimuthal Lorentz force driven by radial eddy currents "leaking" from the centre of the vortex. This effect is schematically represented on a pair of counter-rotating vortices in figure 1 (a). From (9), The intensity of these currents is proportional to the gradient of velocity in the core, which decreases away from the bottom wall. At a distance l'_z , the total vertical current injected in the core at $z = 0$ is exhausted and the vortex dies out. l'_z can be found by taking three times the curl of (1) and using (7):

$$\sigma B^2 \partial_{zz}^2 \omega_z = \rho\nu \nabla^4 \omega_z. \quad (10)$$

Assuming that derivatives along \mathbf{e}_z are of the same order or smaller than radial ones, it follows that:

$$\frac{l'_z}{l_\perp} \sim \frac{l_\perp}{h} Ha = \frac{l_\perp}{\delta_H}. \quad (11)$$

If $l_z < h$, the current injected through the electrode doesn't reach the upper wall and spreads between the core and the bottom boundary layer,

$$I = I_c + I_b, \quad (12)$$

where the total current that feeds meridional currents $I_c \sim 2\pi l_\perp l'_z J_r$ can be estimated from (9) by noting that $\nabla^2 \sim l_\perp^{-2}(1 + \delta_H^2/l_\perp^2) \sim l_\perp^{-2}$ implies $J_r \sim \rho\nu U_b/(Bl_\perp^2)$. Using (8), it comes that the injected current spreads equally between the core and the boundary layer ($I_b = I_c = I/2$), and so the corresponding velocity outside the bottom Hartmann layer is

$$U_b \sim \frac{1}{2} \frac{I}{2\pi l_\perp \sqrt{\sigma\rho\nu}}. \quad (13)$$

Based on this result, we shall define two distinct Reynolds numbers to characterise respectively the forcing and the measured flow intensity:

$$Re^0 = \frac{K\Gamma}{2\nu} \quad \text{with} \quad \Gamma = \frac{I}{2\pi\sqrt{\sigma\rho\nu}}, \quad (14)$$

$$Re^b = \frac{U_b l_\perp}{\nu}. \quad (15)$$

Γ is the circulation created by injecting current I through a single electrode, whereas K accounts for more complex patterns of current injection. For a single vortex $K = 1$; in a square vortex array of alternate spin and step L_i , the velocity induced between two electrodes is $2\Gamma/(L_i/2)$ and so $K = 4$, as in Klein & Pothérat (2010). In regimes where three-dimensionality is driven by viscous effects, these non-dimensional numbers thus obey a scaling of the form:

$$Re^b \simeq C_0 Re^0, \quad (16)$$

which is of the same form as the scaling for quasi-two dimensional flows. Both are inertialess in the sense that inertial effects in the bulk are negligible. In (16) and the remainder of this section, all constants C and D with various indices are real scalars, expected to remain of the order of unity. The physical mechanism underlying (11) and (16) is the same as that discovered by Ludford (1961) and Hunt *et al.* (1968): it explains the presence of a zone of stagnant fluid in regions attached to solid obstacles and extending over a distance of the order of Ha along \mathbf{B} . Hunt's wake, as it was later called was found in the numerical simulations of Dousset & Pothérat (2012) and in the recent experiments of Andreev *et al.* (2013). Alpher *et al.* (1960), also reported the existence of a similar wake attached to a conducting strip placed in a free surface channel flow.

This theory holds in the inertialess limit $N \gg 1$. When $N \lesssim 1$, Pothérat *et al.* (2000) and Davidson & Pothérat (2002) showed that the Hartmann layer becomes a Hartmann-Bodewädt layer and differential rotation between this layer and the bulk drives meridional recirculations akin to Ekman pumping. Furthermore, it was recently discovered that if $\partial_z u_\theta$ becomes of the order of u_θ/R , an axial pressure gradient builds up along the axis of the vortex that drives a strong flow towards the wall there (Pothérat *et al.* (2013)). When such a meridional flow is present, inertia scales as $\mathbf{u} \cdot \nabla \omega \sim u_\theta u_r / R^2$ and if Re is large enough, the scaling in (11) isn't expected to hold anymore.

2.4 Three-dimensional electrically driven non-axisymmetric vortex

When axisymmetry is broken, either because of the influence of neighbouring vortices or because of unsteadiness, then strong inertia may act in the core with $u_r \sim u_\theta \sim U_b$, and therefore $\mathbf{u} \cdot \nabla \omega \sim U_b/R^2$. By virtue of (9) it must be balanced by a Lorentz force and this pulls some of the current injected at the electrode into the bulk of the flow. Then, neglecting viscous effects in (9), and using (6), as in section 2.3, it comes that the length $l_z^{(N)}$ over which the vortex extends into the core scales as

$$\frac{l_z^{(N)}}{l_\perp} \sim N^{1/2}. \quad (17)$$

This relation also expresses that the vortex length l_z is determined by the the balance between momentum diffusion along \mathbf{B} and inertia, which can also be written as $N_t(l_\perp) = N(l_\perp/l_z) \sim 1$. Using the same approach as for the axisymmetric vortex of section 2.3, and still considering that $l_z < h$, we note that the core current scales as $J_r \sim \rho U_b^2 l_\perp^{-1} B^{-1}$, and arrive at a new scaling for the velocity outside the bottom boundary layer:

$$U_b \sim \frac{1}{1 + Re_b^{1/2}} \frac{I}{2\pi l_\perp \sqrt{\rho \sigma \nu}}. \quad (18)$$

For $Re \gg 1$, the inertial regime is thus characterised by a scaling of the form:

$$Re^b \simeq C_b^{(N)} (Re^0)^{2/3}. \quad (19)$$

Velocity and current distributions are qualitatively similar to those represented in figure 1, but differ from the viscous case of section 2.3 in how they scale with Re^0 . A similar distinction between viscous and inertial regimes was observed experimentally by Duran-Matute *et al.* (2010) in electrolytes flows driven by passing an imposed current through an inhomogeneous magnetic field. In this case however, the current was not influenced by the flow and so the Lorentz force acted as an externally imposed force, as opposed to the case considered here where the Lorentz force does result from a two-way coupling between velocity and electric currents. In the viscous regime, they found a scaling consistent with (8), whereas in our notations, the Reynolds number in their inertial regime scaled as $Re \sim (Re^0)^{1/2}$. It stemmed from a different forcing mechanism whereby the electric current, and therefore the Lorentz force, spread across the whole fluid layer instead of being largely confined to the boundary layers, as here at high Hartmann numbers. The Lorentz force was then directly balanced by inertial terms, which in our notations translates as:

$$\frac{IB}{hl_\perp} \sim \frac{\rho U_b^2}{l_\perp}, \quad (20)$$

and hence the aforementioned scaling.

2.5 Three-dimensional flows bounded by two Hartmann walls

Let us now consider the influence of the Hartmann wall present at $z = h$. If, as in the previous section, $h > l_z$, then only weak residual flows and currents exist in its vicinity. The influence of the wall on the flow will be minimal and either of scalings (8) or (18) are expected to hold. If, on the other hand $h < l_z$, the current injected through an electrode mounted at the bottom wall separates in three components instead of two (when $h > l_z$): the first one, I_b flows from the electrode directly into the bottom Hartman layer and satisfies $U_b = I_b/(2\pi l_\perp \sqrt{\sigma \rho \nu})$ as previously. The second one is pulled into the core either by viscous or inertial forces, depending on the values of Ha and N . Unlike when $l_z < h$, a residual current I_t remains at $z \sim h - \delta_H$, that didn't flow

into the Hartmann layer and wasn't pulled into the core by inertial or viscous effects either: the top wall "cuts" the vortical structure at $z = h$, where a significant flow U_t still exists, that satisfies $U_t \simeq I_t / (2\pi l_\perp \sqrt{\sigma \rho \nu})$, by virtue of (6).

In the inertialess regime, $N \gg 1$ and (1) expresses that the current pulled into the core for the Lorentz force to balance viscous forces there is $I_c \sim 2\pi l_\perp \rho \nu h U_b / (Bl_\perp)$. Then, since $I = I_b + I_c + I_t$, it comes that the inertialess scaling (16) found for Re_b in the absence of the top wall remains valid and

$$U_t \sim U_b \left(1 - \frac{h^2}{l_\perp^2} Ha^{-1} \right). \quad (21)$$

Using Re^t , a Reynolds number based on the top velocity U_t , this yields a non-dimensional scaling of the form:

$$Re^t \simeq C_t^{(Ha)} Re^0 \left(1 - D_t^{(Ha)} \frac{h^2}{l_\perp^2} Ha^{-1} \right). \quad (22)$$

The top wall thus affects the distribution of current in the core, mostly in its vicinity but not near the bottom wall.

The same reasoning applies to the inertial regime ($N \lesssim 1$), where this time, the current pulled into the core must balance inertial forces, instead of viscous ones. It then accordingly scales as $I_c \sim 2\pi l_\perp h \rho U_b^2 / (Bl_\perp)$. Again, the velocity field near the bottom wall is unaffected by the presence of the top wall: scaling (18) for the velocity outside the bottom Hartmann layer still holds while the scaling for the top velocity outside the top Hartmann layer becomes:

$$U_t^N \sim U_b \left(1 - \frac{h^2}{l_\perp^2} N^{-1/2} \right) = U_b \left(1 - N_t^{-1/2}(l_\perp, h) \right), \quad (23)$$

and from (19) this expresses non-dimensionally as:

$$Re^t \simeq C_t^{(N)} (Re^0)^{2/3} \left(1 - D_t^{(N)} N_t^{-1/2}(l_\perp, h) \right). \quad (24)$$

Importantly, Sommeria & Moreau (1982) argues that in a turbulent flow where inertia-driven three-dimensionality affects a wide range of scales, a cutoff lengthscale l_\perp^c exists that separates quasi-two dimensional from three-dimensional structures. The expression they find for l_\perp^c is recovered for $l_z^{(N)} = h$ in (17).

$$\frac{l_\perp^c}{h} \sim N^{-1/2} = N_L^{-1/3}, \quad (25)$$

where N_L is an interaction parameter built on the large scales L . An analogous scale exists below which viscous effects always drive three-dimensionality. From (11), this "viscous" cutoff scale expresses as:

$$\frac{l_\perp^c}{h} \sim Ha^{-1/2}, \quad (26)$$

which corresponds to the thickness of Shercliff layers.

2.6 Symmetric vs. antisymmetric three-dimensionality

Equation (9) imposes that inertial or viscous effects in the core pull a horizontally divergent current there and induce a variation of vertical current. It imposes, however, no constraint on the direction in which this current travels along \mathbf{B} . This shall be decided by the problem boundary conditions. In the examples of figures 1 (a), (b) and (c), the current enters and leaves the domain at two electrodes located at the bottom wall. The topology of the electric current lines must ensure that the circuit is closed whilst satisfying this topological constraint and this forces the current to flow

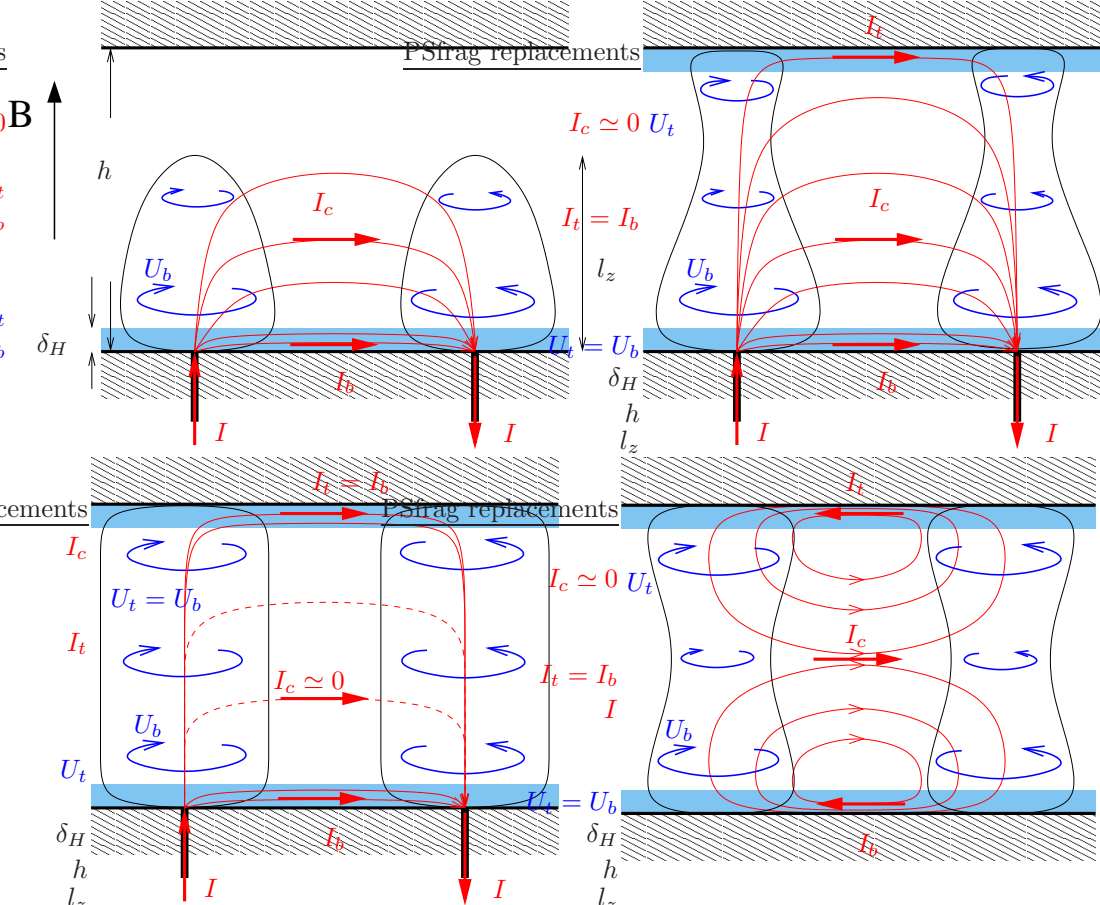


Figure 1: Schematic representation of generic flow configurations in a channel with a transverse magnetic field. Hartmann layers are represented in light blue, paths of electric current in red, and fluid flow in blue. (a) $l_z \ll h$: the injected current spreads between the Hartmann layer and the core where the Lorentz force it generates balances either viscous or inertial forces. (b) $l_z \gtrsim h$: same as (a) but part of the injected current flows into the top Hartmann layer. The flow is 3D and influenced by the top wall. (c) $l_z \gg h$: the current spreads equally between top and bottom Hartmann layers, with practically no leak into the core: the flow is quasi-two dimensional. (d) symmetrically three-dimensional structures, not attached to electrodes and where eddy currents in the core are equally sourced from both Hartmann layers.

as sketched. A structure not attached to an injection electrode may, by contrast, not necessarily exhibit the asymmetry imposed by the electrode and the current that loops in the core may be sourced from either Hartmann layers. In this case, Poth erat *et al.* (2000)'s asymptotic analysis of a symmetric channel (with no injection electrode) shows that when N decreases from infinity, the first form of three-dimensionality encountered is symmetric, with a velocity profile that is quadratic in z . The underlying mechanism was indeed the same as in sections 2.4 and 2.5, except that eddy currents feeding the core current took source equally in the top and bottom Hartmann layers, as sketched on figure 1 (d).

Symmetric three-dimensionality may still occur in a channel where the flow is driven by injecting current at one wall only. In turbulent regimes indeed, energy is transferred from the mean flow, made of vortices attached to the injection electrodes, to transient structures, not attached to electrodes, in a structure turnover time $\tau_u = l_{\perp}^{\text{mean}}/U_b$, and passed further down the inertial range to smaller structures. After typically $\tau_{2D}(l_{\perp}^{\text{mean}}) = (h/l_{\perp}^{\text{mean}})^2 \rho/(\sigma B^2)$, momentum diffusion by the Lorentz force has erased the original asymmetry of the mean flow and Poth erat *et al.* (2000)'s theory becomes relevant. Depending on their sizes, the associated structures can be either two or three-dimensional, satisfying either (16) or (19) (with Re_b based on their characteristic scales and velocities). By contrast, since the top and bottom velocities must have the same statistical properties out of symmetry, (24) does not apply to symmetrically three-dimensional structures. Note that it is *a priori* possible that symmetrically three-dimensional structure do exist, since from Sommeria & Moreau (1982), for a structure of size l_{\perp} to be three-dimensional, its turnover time must satisfy $\tau_{2D}(l_{\perp}) > l_{\perp}/U(l_{\perp})$. For it to be symmetric, on the other hand, the energy transfer time from the mean flow to it, which is at least $l_{\perp}^{\text{mean}}/U_b$, must be larger than $\tau_{2D}(l_{\perp}^{\text{mean}})$. For $l_{\perp} < l_{\perp}^{\text{mean}}$, $\tau_{2D}(l_{\perp}^{\text{mean}}) < \tau_{2D}(l_{\perp})$, and so depending on the variations of $U(l_{\perp})$, both conditions may be satisfied (for instance if $U(l_{\perp}) \sim U_b$), and symmetric three-dimensionality may be present in turbulent fluctuations.

3 The *FLOWCUBE* Experimental facility

3.1 Mechanical description

The principle of the experiment follows that of Sommeria (1986) on quasi two-dimensional turbulence in which a constant, almost homogeneous magnetic field $\mathbf{B} = B\mathbf{e}_z$ was applied across a square, shallow container of height 0.02 m filled with liquid mercury (the frame origin is chosen at the centre of the bottom wall, with \mathbf{e}_x and \mathbf{e}_y pointing along its edges). In his configuration, the time scale for two-dimensionalisation $\tau_{2D}(l_{\perp})$ for each flow structure of transverse size l_{\perp} was less than 10^{-2} s and much smaller than the structures turnover time $\tau_U(l_{\perp})$. The flow was assumed quasi two-dimensional on these grounds. Unlike this earlier experiment though, the present container is not shallow, but cubic and with inner edge $L = 0.1$ m, with impermeable, electrically insulating walls, except where small electrodes are inserted, either to drive or diagnose the flow. Since Hartmann and Shercliff layers are expected to develop along walls perpendicular and parallel to \mathbf{B} , we shall refer to them as *Hartmann walls* and *Shercliff walls*, respectively (Fig. 2 and Fig. 3). For the lower magnetic field strengths, this corresponds to times $\tau_{2D}(l_{\perp})$ of the order of 1s and therefore much longer than those of Sommeria (1986), and potentially comparable or longer than eddy turnover times. In these conditions, three-dimensionality is expected to be present. The working liquid metal is Gallinstan (also referred to as MCP11), an eutectic alloy of gallium, indium and tin that is liquid at room temperature, with electric conductivity $\sigma = 3.4 \times 10^6$ S/m, density $\rho = 6400$ kg/m³ and viscosity $\nu = 4 \times 10^{-7}$ m²/s. The container is successively filled with argon and vacuumed several times so as to ensure that as little gas as possible remains inside the vessel, and that whatever remains cannot oxide the Gallinstan. This way, the liquid metal is in the

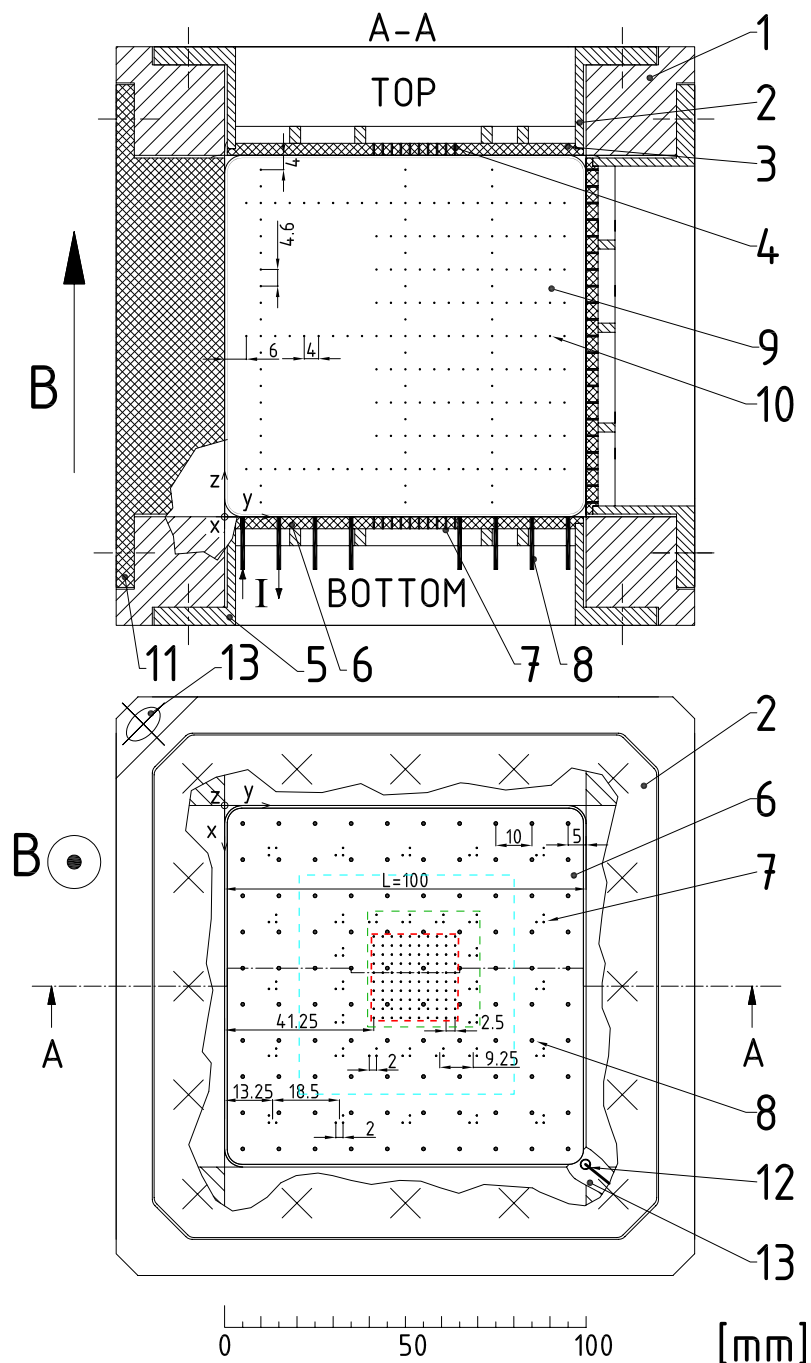


Figure 2: Sketch of the cubic container. Top: cross section. Bottom: top view onto the bottom plate. (1) cubic brazen frame; (2) top-holder with top-electronic board (3) with 196 potential probes (4); (5) bottom-holder with bottom-electronic board (6) with the same set of 196 potential probes (7) as on the top and additional 100 forcing electrodes (8); (9) parallel-electronic board with 195 potential probes (10); (11) side plate; (12) probe for electric potential reference; (13) inlet and outlet to evacuate the container and to fill it with liquid metal. All container walls are electrically insulating, except at the locations of potential probes and current injection electrodes. The central square region with high density of electric potential probes on the Hartmann walls is marked with a red dashed line.

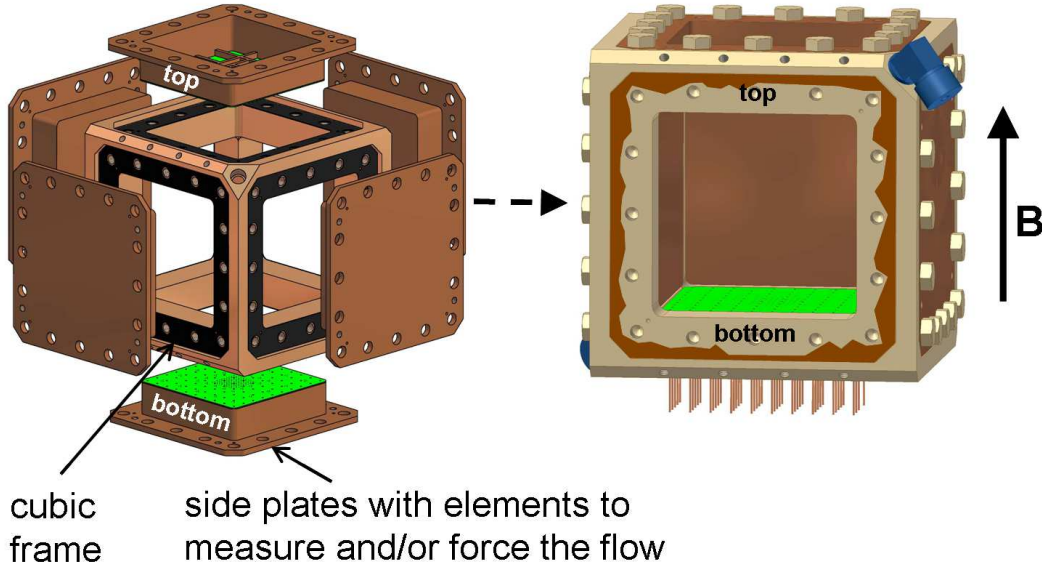


Figure 3: Modular design made of a cubic frame with interchangeable side plates. When modifications on the experiment are required, these plates can be easily swapped to exchange flow forcing and flow measurement systems. Left: open container with side plates unmounted. Right: closed container where the front plate is only partly represented to allow for a view into the container.

tightest mechanical and electrical contact with the walls and all wall-embedded electrodes. Once filled with Gallinstan, the container is subjected to a magnetic field $B\mathbf{e}_z$ by being placed at the centre of the cylindrical bore of a superconducting solenoidal magnet. Magnetic field strengths $B \in [0.1, 5]\text{T}$ with maximum inhomogeneity of 3% along \mathbf{e}_x , \mathbf{e}_y , and \mathbf{e}_z and with corresponding *Hartmann* numbers $\text{Ha} \in [364, 18220]$ are achieved.

The flow entrainment relies on the same principle as in Sommeria (1986) and Klein *et al.* (2009)'s experiments. A DC electric current in the range $I \in [0 - 300]\text{A}$ is injected at the bottom *Hartmann* wall located at $z = 0$ (Fig. 2), through a lattice of either $n = 100$ or $n = 16$ electrodes, each of diameter 1 mm (The terminology "top" and "bottom" is used for convenience since gravity plays no relevant role in this experiment). The forcing geometry thus consists of a square array of either 10×10 or 4×4 electrodes respectively spaced by distances either $L_i = 0.01$ m or $L_i = 0.03$ m (non-dimensionally, $\lambda_i = L_i/h = 0.1$ or $\lambda_i = 0.3$), both centred on the bottom *Hartmann* plate. The electrodes are made of copper and gold plated, which provides a good electrical contact with the Gallinstan. They are embedded into the bottom *Hartmann* wall located at $z = 0$, and mounted flush so that they do not protrude into the liquid metal and bring no mechanical disturbance into the flow. At their other end they are connected to either pole (positive and negative) of a regulated DC power supply through a dedicated switchboard system. This switchboard system makes it possible to connect each of the 100 available electrodes to either the positive or the negative pole of the DC power supply or to leave it open-ended. The 10×10 and 4×4 arrays are obtained by alternately connecting all the electrodes to either pole (10×10), or by leaving 2 unconnected electrodes between one connected to the positive pole and one connected to the negative pole (4×4). For low injected electric current I , the base flow consists of vortices of diameter L_i spinning in alternate directions as in Sommeria (1986)'s experiment.

Since all electrodes are connected to a single power supply, particular attention was paid to

ensure that the same, constant current intensity I passed through all electrodes, despite random fluctuations in the contact resistance between the electrode surface and the liquid metal. These fluctuations with amplitudes of the order of $10^{-2} \Omega$ can lead to an irregular current distribution resulting into an ill-controlled forcing. By adding a constant ohmic resistance of $2\Omega \pm 0.25\%$ to all 100 electric circuits, the impact of this effect on the uniformity of the forcing becomes negligible. Each 2Ω -resistance dissipates a maximal power of 100W, which limits the injected electric current per electrode to about 7A. To evacuate heat, they are mounted on water cooled aluminium plates.

3.2 Electric potential measurements

The flow is analysed by measuring electric potential ϕ locally, at probes that are embedded in the container walls. Each electric potential is obtained with respect to a reference taken in the thin inlet pipe located in a corner of the vessel, where the liquid metal is always at rest (see Fig. 2). Each probe consists of a gold plated copper wire of 0.2mm in diameter mounted flush in the container wall, in the same way as the current injection electrodes are. This way, they incur no mechanical disturbance on the flow and practically no electrical one either. 196 of these probes are embedded in the $x - y$ plane, in bottom ($z = 0$) and top ($z = h$) *Hartmann* walls and 195 probes in the $y - z$ plane at one of the parallel walls where $x = 0$. The sets of potential probes embedded in the top and bottom *Hartmann* walls are mirror symmetric and precisely aligned opposite each other along magnetic field lines. Near the centre of the Hartmann walls, probes are positioned in a dense 10×10 grid of spacing $\Delta x = \Delta y = \Delta = 2.5\text{mm}$ to map the smaller spatial variations of potential. Mid-size and box-size structures are captured by measurements on sets of three probes (distant by $\Delta x = \Delta y = 2 \text{ mm}$ from one another so as to record local variations of ϕ along \mathbf{e}_x and \mathbf{e}_y), around the centre array and further out close to the Shercliff walls themselves (Fig. 2). On the Shercliff wall at $x = 0$, probes are respectively spaced by $\Delta y = 4\text{mm}$ and $\Delta z = 4.6\text{mm}$ along \mathbf{e}_y and \mathbf{e}_z . Signals recorded there give an insight on the structure of the flow along the magnetic field lines. Printed electric circuits at the flip side of each wall convey the signals from all probes to connectors leading to a high precision single-ended 736-channel acquisition system, manufactured and tailored for this particular experiment by company NEUROCONN¹. Since the signals can be of the order of $10\mu\text{V}$, each channel features a low-noise amplifier with gain 111. All signals are then synchronously sampled to 24-bit precision at a frequency of 128Hz. Digital signals are optically transmitted to a PC where they are recorded through a dedicated MATLAB/SIMULINK module. Since frequencies relevant to the flow are typically expected in the range $[0, 35] \text{ Hz}$, each channel is fitted with a low pass filter of cut-off frequency of 45 Hz. The peak-to-peak background noise that remains on the filtered signal is less than $2\mu\text{V}$, and this determines the precision of the measurement system. The measurement chain provides real-time simultaneous time series of electric potential in 736 locations spread between the top and bottom Hartmann walls (thereafter denoted ϕ_b and ϕ_t) and on one of the Shercliff walls. At the Hartmann walls, gradients of electric potential shall be determined from a first order approximation:

$$\nabla_{\perp}\phi = \frac{1}{\Delta} \begin{bmatrix} \phi(\mathbf{r} + \Delta\mathbf{e}_x) - \phi(\mathbf{r}) \\ \phi(\mathbf{r} + \Delta\mathbf{e}_y) - \phi(\mathbf{r}) \end{bmatrix} + \mathcal{O}(\Delta^2). \quad (27)$$

Electric potentials measured on Hartmann walls can also be related to the velocity field \mathbf{u}^c in the bulk of the flow just outside the Hartmann layer using Ohm's law there, and neglecting variations of potential across the Hartmann layers, which are of the order of Ha^{-2} . For the bottom wall,

$$\mathbf{u}^c = B^{-1}\mathbf{e}_z \times \nabla_{\perp}\phi_b + (\sigma B)^{-1}\mathbf{e}_z \times \mathbf{J}^c, \quad (28)$$

¹<http://www.neuroconn.de/profile/>

where \mathbf{J}^c is the current density just outside the Hartmann layer. In quasi two-dimensional flows, $J^c \sim \sigma B u^c Ha^{-1}$ can be neglected. (28) then provides an indirect measurement of the velocity field, which has been widely used in MHD experiments thin fluid layers (Alboussière *et al.* (1999)). Kljugin & Thess (1998) further noticed that in this case, the streamfunction in the bulk becomes proportional to ϕ_b and so iso-lines of ϕ_b provide a direct visualisation of flow patterns. When the flow becomes three-dimensional, however, J^c becomes larger but still depends on the mechanism which pulls current in the core. For instance, from section 2, when inertial effects are present, $J^c = \mathcal{O}(N^{-1})$, so even in this case, flow patterns can still be identified and velocities estimated from (28), albeit with a precision that decreases with N^{-1} (see Sreenivasan & Alboussière (2002) where errors involved in this measurement technique are estimated). We shall follow this strategy to identify flow regimes in section 4 and to test the scaling laws derived in section 2 against our measurements. The measure of three dimensionality, on the other hand requires more precision but doesn't directly necessitate the knowledge of \mathbf{u} . Indeed, in a quasi-two dimensional flow, measurements of electric potential and their gradient taken at top and Hartmann walls should be fully correlated, whereas any trace of three-dimensionality should translate into a loss of correlation between these quantities. On these grounds, the quantification of three-dimensionality in section 6 shall rely on correlations of electric potential gradients between top and bottom Hartmann walls.

3.3 Experimental Procedure

Experiments are performed at a constant magnetic field (constant Ha). Starting from a flow at rest, the current per electrode, and hence Re^0 , is increased in about 20 steps, spread logarithmically between 0 and 6A. Additional measurements in steps refined between 0.01A and 0.1A were made in the vicinity of transitions between regimes to detect critical values of Re^0 precisely. At each step, electric potentials were recorded in a statistically steady state, which was deemed reached after typically $5\tau_H$, where the Hartmann friction time $\tau_H = h^2/(2\nu Ha)$, which characterises quasi-dimensional dynamics (Sommeria & Moreau (1982)), is much longer than τ_J which characterises three-dimensional effects. Records extended over a maximum of 7 to 10 min, imposed by limitations of the cooling system for the superconducting coil. To ensure stability of the magnetic field, the magnet was operated in "persistent mode", *i.e.* with the coil disconnected from its power supply. Variations of magnetic fields were not measurable over one day.

4 Overview of flow regimes

Varying parameters Re , Ha and λ_i , reveals a complex landscape of steady and unsteady flow regimes, visible from the time-dependent contours of electric potentials along both Hartmann walls. We shall first establish a detailed map of these regimes in the space of parameters, and initially track the most visually conspicuous traces three-dimensionality.

4.1 Array of 10×10 vortices ($\lambda_i = 0.1$)

The flow regimes attained in this configuration were first described in Klein & Pothérat (2010). We shall here discuss their main features in the light of the theory from section 2, and also highlight how those of the 4×4 array differ from them. The corresponding stability diagram in (Ha, Re^0) space is represented on figures 4 and 5.

At high Ha , weak forcing induces a steady quasi-two dimensional square array of 100 vortices aligned with the position of the injection electrodes, and whose spin corresponds to the sign of the injected current. Unsteadiness appears at $Re_J^0 \simeq 0.164Ha$ under the form of periodic pairing of vortex of same spin. As Re is further increased, more quasi-two dimensional modes are excited until

the flow reaches a state of quasi-two dimensional turbulence. The ratio $R_h^0 = Re_I^0 / Ha$ represents the ratio of the Lorentz force to inertia in quasi-two dimensional flows, for which the current in the core drops to $J \sim \sigma B U_b Ha^{-1}$. This phenomenology is exactly that observed by Sommeria (1986) in a shallow layer of mercury at much lower values of Ha . The contours of ϕ obtained on both Hartmann walls, however, provide an evidence that the flow is indeed quasi-two dimensional in this regime. This picture remains valid for all measurements at $Ha > 7500$.

Lowering the values of Ha , the contours of ϕ reveal the first traces of three-dimensionality in the unsteady regime. Although the contours on both Hartmann walls continue to be topologically identical, the values of ϕ at the top wall, and the flow intensities near it, are noticeably lower than their counterparts measured at the forcing wall. We call this form of three-dimensionality *weak*, as opposed to *strong* three-dimensionality for which contours of ϕ in different planes orthogonal to \mathbf{B} are not topologically identical. Weak three-dimensionality is easily understood in the light of the mechanisms predicted theoretically in section 2.5 as it reflects that inertial or viscous effects in the core incur a velocity drop away from the bottom wall, where the flow is forced. Distinguishing inertial from viscous effects is, however, not possible through streamline visualisation only and this shall require quantitative measurements from the following sections. Nevertheless, the fact that weak three-dimensionality is present in unsteady flows and not just in steady vortices gives an early indication that the mechanisms outlined by reasoning on single vortices are at play in more complex structures too. When three-dimensional mechanisms are visible from the streamlines, typically for $Ha \leq 7500$, which we shall term as *low Ha region*, the dependence $Re_I^0(Ha)$ becomes non-linear and two extra steps enter the succession of flow regimes. Firstly, the flow re-stabilises into a steady state at $Re_{st}^0 > Re_I^0$, and secondly, it destabilises again at $Re_{II}^0 > Re_{st}^0$. In the interval $3500 < Ha \leq 7500$, the re-stabilised state consists of weakly three-dimensional paired vortices visible on figure 5, but the most remarkable state was found at $Ha = 1820$, where strong three-dimensionality is already present as soon as $Re^0 > Re_I^0$. The vortices, which are weakly three-dimensional for $Re^0 < Re_I^0$, do start pairing as soon as $Re^0 > Re_I^0$, as at higher Ha . Pairing, however, only takes place near the top wall as the bottom wall still shows the steady 10x10 array. In the second steady state, while the trace of the 10x10 array of vortices on the bottom wall remains topologically identical to that in the first steady regime, contours near the top wall display the trace of a 5x5 array. This implies that strong three-dimensionality is present in a *steady* state, in structures that connect four vortices near the bottom wall to one near the top wall.

4.2 Array of 4×4 vortices ($\lambda_i = 0.3$)

When the injection scale is changed to $\lambda_i = 0.3$, the nonlinear part of the curve $Re_I^0(Ha)$, (*low Ha region*) is shifted to values of Ha below ~ 1450 . The steady state exhibits the same features as when $\lambda_i = 0.1$, but this time, no other steady state was found when increasing Re^0 progressively. Instead, the initial vortex pairing at $Re \gtrsim Re_I^0$ becomes progressively more chaotic until a fully turbulent state is reached.

The region $1450 < Ha < 3640$ of the diagram corresponds essentially to the the high Ha region identified at $\lambda_i = 0.1$. The stability of the array is dominated by quasi-two dimensional dynamics, and the neutral stability curve $Re_I^0(Ha)$ is linear, with a slope corresponding to $R_h^0 = 2.36$. This value, noticeably higher than for $\lambda_i = 0.1$, reflects the influence of the side walls, which exert considerable friction on 12 of the 16 electrically driven vortices (*vs.* 38 of the 100 vortices driven at $\lambda_i = 0.1$). This damping considerably lowers the velocity of the external vortices and thus increases the stability of the whole array. This effect could also be noticed through considerably lower values of electric potential near the side walls than near the centre of the box.

The most distinctive part of the stability diagram for $\lambda_i = 0.3$ is found at $Ha > 3640$. In this region, destabilisation of the array through vortex pairing still sets in at $R_h^0 = 2.36$, but not on a steady base flow. Two additional instabilities indeed occur at $Re^0 < Re_I^0$. The first one is a

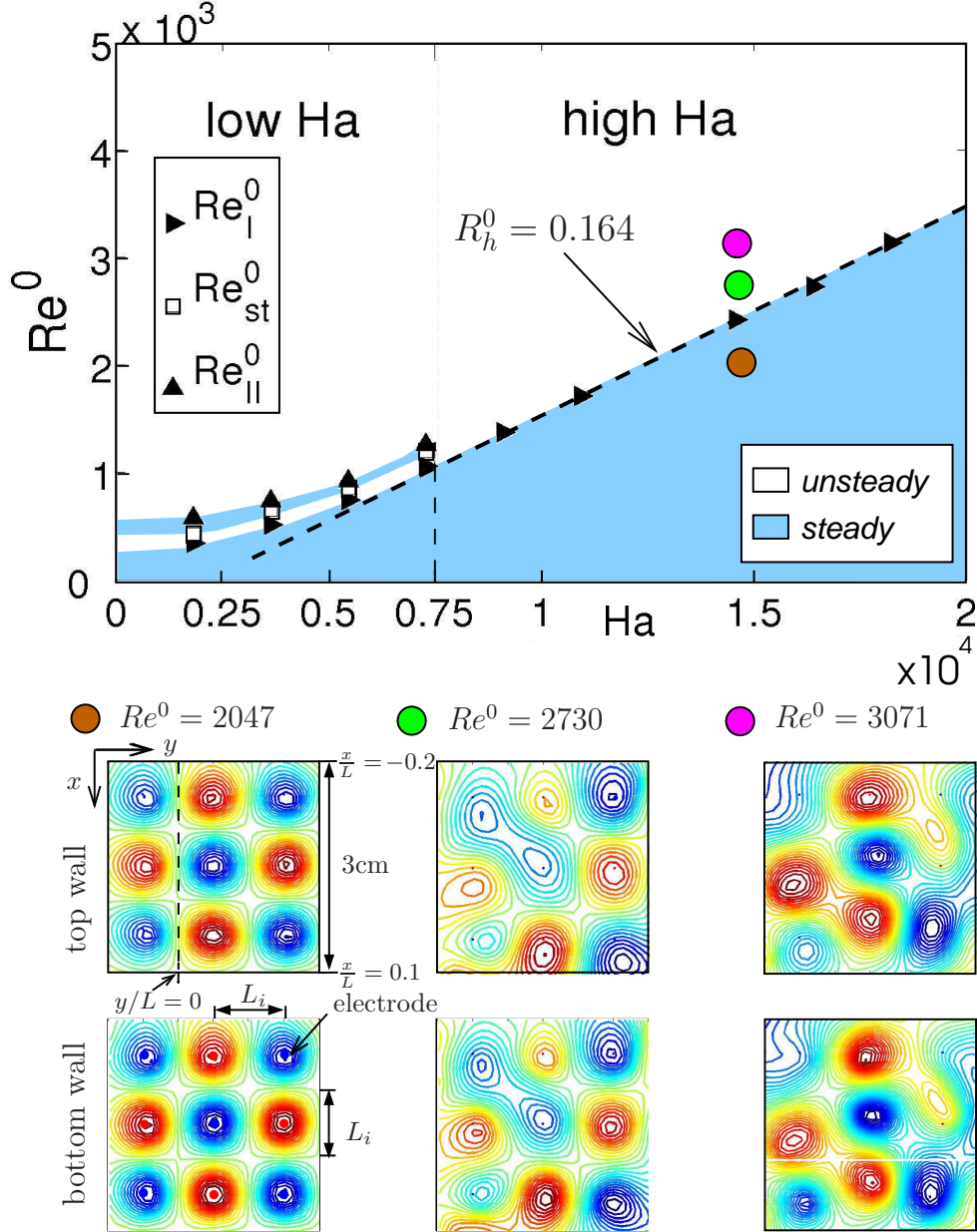


Figure 4: Stability diagram for forcing scale $\lambda_i = 0.1$, giving critical Reynolds numbers $Re^0_I(Ha)$, $Re^0_{st}(Ha)$ and $Re^0_{II}(Ha)$ vs. Ha and snapshots of iso- ϕ lines in the central square (in red in figure 2, at the bottom and top Hartmann walls at $Re^0 \lesssim Re^0_I$ and $Re^0 \gtrsim Re^0_I$ for $Ha = 1.458 \cdot 10^4$, for which the flow is quasi-2D

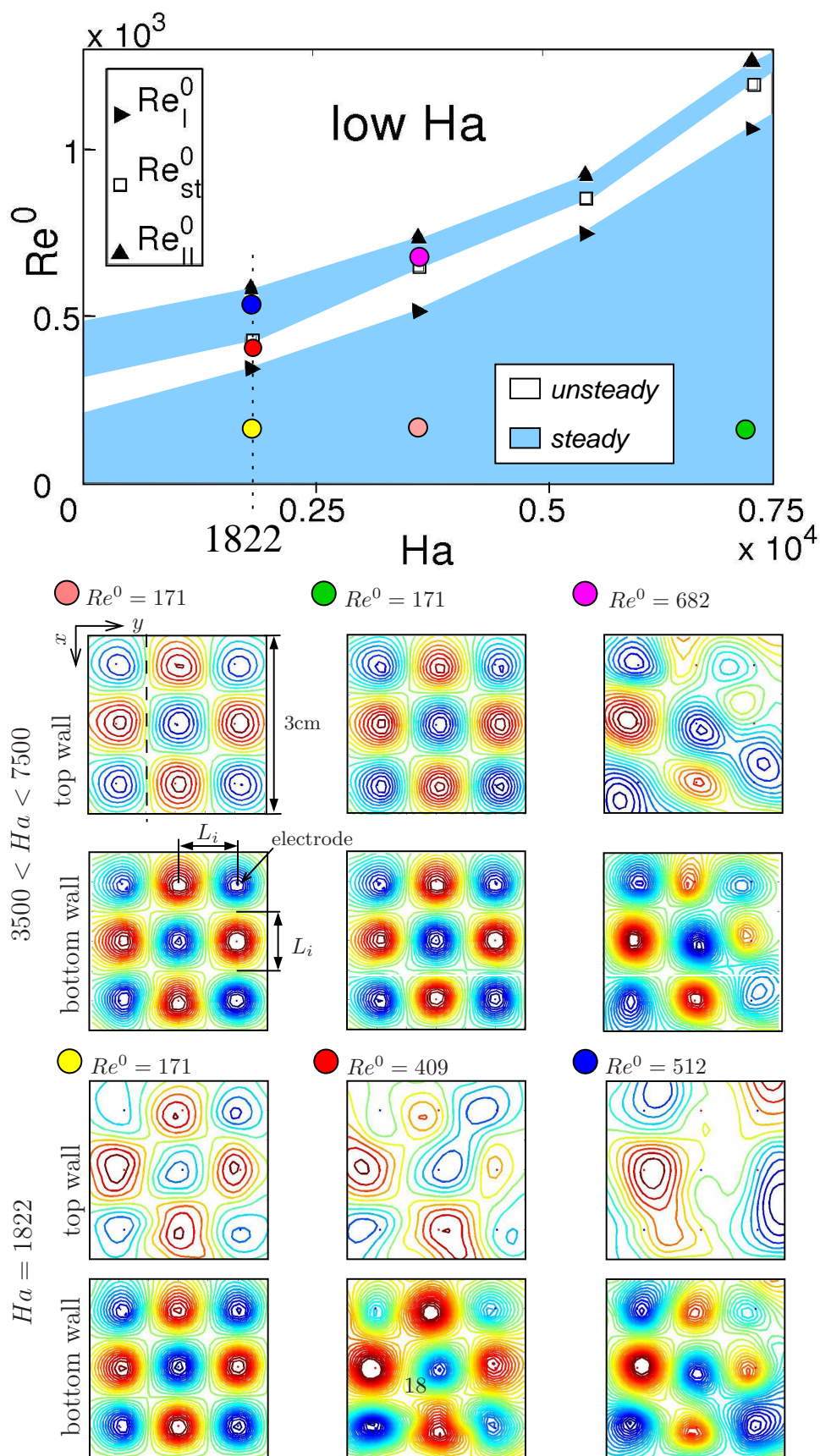


Figure 5: Bottom: magnification of the stability diagram for $\lambda_i = 0.1$ in the low Ha region and Re^0 values (displayed next to the data points) for $Ha = 1822$ for which $\lambda_i = 0.25$.

second type of vortex pairing occurring exclusively in a range, $Re_{III}^0(Ha) \leq Re^0 \leq Re_{IV}^0(Ha)$, where $Re_{IV}^0(Ha) < Re_I^0(Ha)$ (see figure 6). It differs from that observed at $Re^0 \geq Re_I^0$, through a significantly lower frequency, but preserves quasi-two dimensionality and remains periodic, with a single frequency peak in the frequency spectra obtained from the time-dependent electric potentials throughout the whole interval $[Re_{IV}^0(Ha), Re_I^0(Ha)]$. By contrast, when Re^0 is increased beyond Re_I^0 , further modes appear and the flow becomes quickly chaotic. Re_{III}^0 and Re_{IV}^0 vary linearly with Ha , with respective values of R_h^0 of 1.62 and 1.78: this scaling again betrays mechanisms driven by two-dimensional inertia, as for the instability occurring at Re_I^0 . Unlike the re-stabilisation phenomenon observed at $Re^0 = Re_{st}^0$ in the low Ha regimes at $\lambda_i = 0.1$, however, the shutdown of this pairing mode at $Re^0 = Re_{IV}^0$ does not lead to any three-dimensional steady structure. In fact, it doesn't even lead to a steady flow.

Indeed, the second instability sets in a $Re^0 = Re_V^0(Ha) < Re_{IV}^0(Ha)$, and persists at $Re^0 > Re_{IV}^0$. Its signature in the frequency spectra of $\phi(t)$ is also a single peak, but of frequency at least an order of magnitude higher than that of the pairing at $Re^0 = Re_I^0$. Furthermore, unlike other instabilities at high Ha , $Re_V^0(Ha)$ is not linear but rather of the form $Re_V^0(Ha) \simeq Ha^\alpha$ with $0 < \alpha < 1$. The ratio $Re^0/Ha^{1/2}$ would correspond to a critical Reynolds number built on the thickness of vortex cores or Shercliff layers (Sommeria (1988)). Furthermore, an inspection of contours of the amplitude of this mode near the bottom wall revealed that it was mostly located near the former. The radial velocity profile of electrically driven vortices indeed exhibits an inflexion point satisfying Fjortoft's criterion at $r \gtrsim Ha^{1/2}$ (Poth erat *et al.* (2000); Schmid & Henningson (2001)) that could explain such a scaling. Unlike vortex pairing mechanisms, this instability generates vorticity at a much smaller scale than the injection scale (of the order of $Ha^{-1/2}$, rather than λ_i), which would explain the high frequency observed. Further experiments targeting this instability would be required to confirm this hypothesis, and to determine α precisely. Nevertheless, for the purpose of the present paper, we shall only notice that this particular instability does not lead to visible three-dimensionality in the contours of ϕ . Yet, if the high frequencies are indeed the trace of vortices of scale $\sim Ha^{-1/2}$, then according to the theory in section 2.3, such vortices introduce a small amount of viscosity-driven three-dimensionality, since at such small scale, the Lorentz force is balanced by viscous friction in the (x, y) plane. For $Ha \gtrsim 7 \times 10^4$, $Re_V^0(Ha) < Re_{III}^0$, so this instability marks the transition to unsteadiness. At $Ha = 3640$, Re_V^0 is only just smaller than Re_I^0 and for $Ha < 3640$, vortex pairing develops at lower Re^0 and marks the transition to unsteadiness.

The regimes inventorised in this section revealed that three-dimensionality could significantly alter the instability mechanisms leading to turbulence and create regimes not observed in purely quasi-two dimensional flows. Its influence turned out to be more important for smaller injection scales. We were also able to distinguish *weak* and *strong* three-dimensionality first identified by Klein & Poth erat (2010). For the purpose of the present work, we shall now leave the precise analysis of these instabilities open for further studies and focus on quantifying three-dimensional mechanisms.

5 Quasi-two dimensionality and viscosity-driven *vs.* inertia-driven three-dimensionality

5.1 Scalings for quantities measured at the bottom Hartmann wall (where current is injected)

We shall now seek evidence of the three-dimensional effects foreseen in section 2 in the regimes we just identified. These were characterised by scaling relations between bulk velocities near top and bottom Hartmann walls, and the injected current per electrode I . Velocities cannot be directly

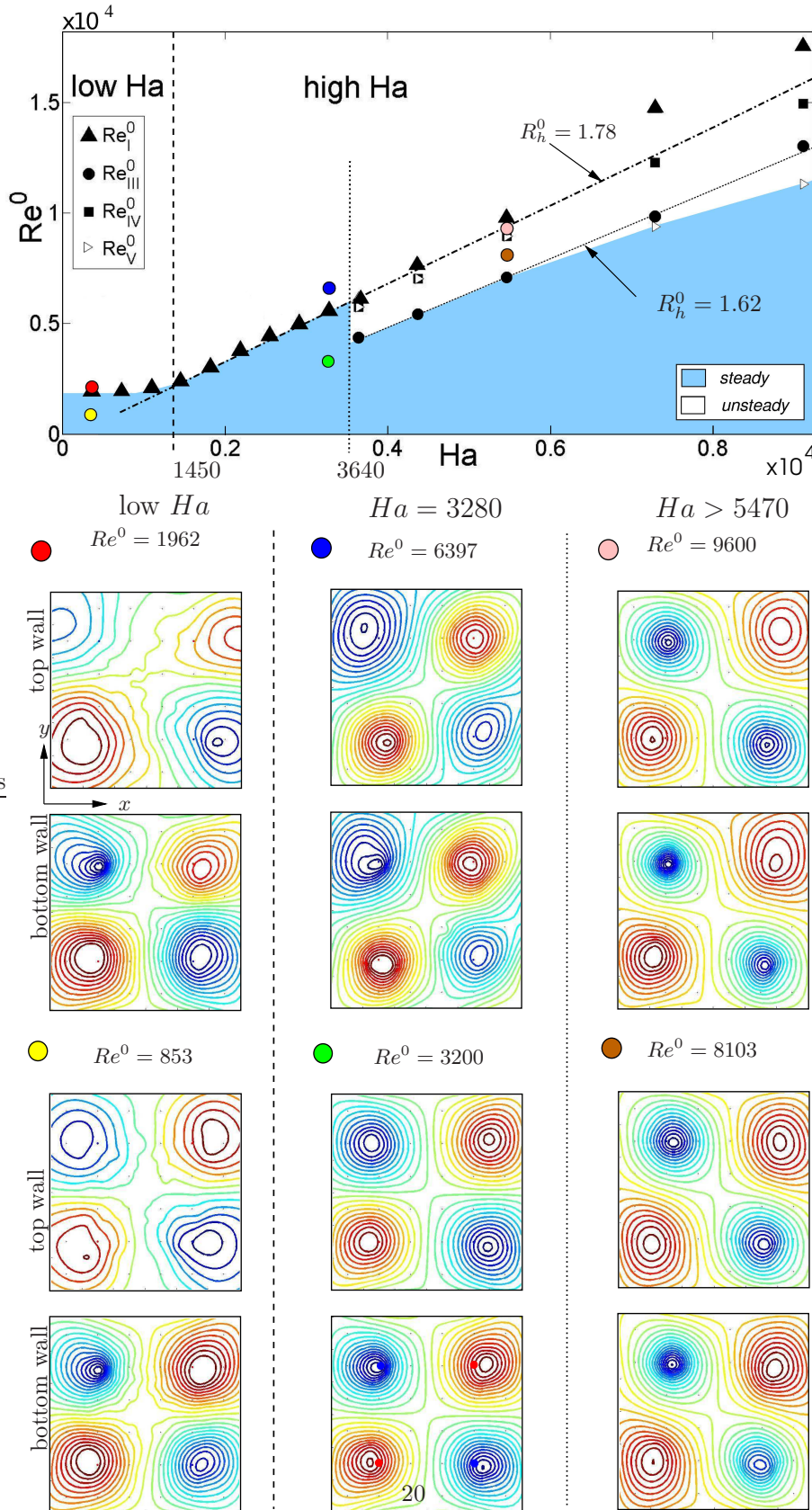


Figure 6: Stability diagram for forcing scale $\lambda_i = 0.3$, giving critical Reynolds numbers $Re_I^0(Ha)$, $Re_{III}^0(Ha)$, $Re_{IV}^0(Ha)$ and $Re_V^0(Ha)$ vs. Ha and snapshots of iso- ϕ lines, in the greater central square (marked in light blue in figure 2) at the bottom and top Hartmann walls in regimes between $10^3 < Ha < 10^4$ and $10^2 < Ha < 10^3$.

measured in the experiment, but can be estimated using (30), from measurements of $\nabla_{\perp}\phi$ at the Hartmann walls. The error incurred in doing so is proportional to the ratio between the current density in the core and that in the Hartmann layer. For these reasons, velocities U_b and U_t , which appeared in the scalings of section 2 were estimated as

$$U_b = B \overline{\langle \|\nabla\phi_b\| \rangle_t}, \quad (29)$$

$$U_t = B \overline{\langle \|\nabla\phi_t\| \rangle_t}, \quad (30)$$

where the over-bar indicates spatial averaging in the central square region (see figure 2), $\langle \cdot \rangle_t$ stands for time-averaging, ϕ_b and ϕ_t are electric potentials measured at the bottom and top wall respectively. Reynolds numbers Re^b and Re^t were built using $l_{\perp} = L_i$ as reference length. We shall also extract scalings for their counterparts $Re^{b'}$ and $Re^{t'}$, built on the RMS of velocity fluctuations near the top wall, estimated as:

$$U'_b = B \overline{\langle \|\nabla\phi_b - \langle \nabla\phi_b \rangle_t\|^2 \rangle_t^{1/2}}, \quad (31)$$

$$U'_t = B \overline{\langle \|\nabla\phi_t - \langle \nabla\phi_t \rangle_t\|^2 \rangle_t^{1/2}}. \quad (32)$$

Figure 7 shows a graph of Re^b against Re^o over the full range of parameters spanned in our measurements for $\lambda_i = 0.1$ (top) and $\lambda_i = 0.3$ (bottom). For any fixed value of Ha , two regimes clearly stand out and data obtained at different values of Ha all closely collapse into a two single curves respectively for lower and higher values of Re^o . For $\lambda_i = 0.1$, these curves correspond to scalings

$$Re^b \simeq 0.24Re^o \text{ for } Re^o < Re_I, \quad (33)$$

$$Re^b \simeq 1.5Re^{o^{2/3}} \text{ for } Re^o \gg Re_I. \quad (34)$$

The scaling at low Re^o is found exclusively in the steady state, where vortices are mostly axisymmetric, and therefore subject to little inertia. It matches scaling (16), with $C_0 \simeq 0.24$. Since this scaling was expected to hold either in quasi-two dimensional flows or in a flow where three-dimensionality was driven by viscous friction in the core, its validity in all steady regimes suggests that no three-dimensionality driven by inertia is present in the first steady regime. Furthermore, from the qualitative observations of flow patterns in section 4, the reason why this scaling holds at high Ha is rather that the flow is indeed close to quasi two-dimensionality (typically $Ha > 7500$ for $\lambda_i = 0.1$ and $Ha > 4000$ for $\lambda_i = 0.3$). At low Ha , on the other hand, three-dimensionality was visible in the base flow, under the form of differential rotation affecting the base vortices. Thus, the validity of (33) in this regimes suggests that this effect is driven by viscous friction.

When the flow becomes unsteady at $Re^o = Re_I$, inertia suddenly appears and triggers a transition away from the inertialess regime. Viscous effects are however still present and a purely *inertial* regime, in the sense that inertia-driven three-dimensionality dominates, is only reached asymptotically at high Re^o , when the flow is significantly supercritical. Re^b then tends to (34), which matches (19) with $C_b^{(N)} = 1.5$, a law derived under the assumption that three-dimensionality was due to inertial effects in the core. It is noteworthy that for higher Ha , the asymptotic value of Re^b consistently stands slightly under that of (34). A possible reason is that Shercliff layers along the four side walls become very thin in this regime and since they occupy a significant surface, they exert friction on the whole flow. This effect can also be reinforced by secondary flows present at high Re^o (hence at moderate values of N_t), which can transport momentum away from columnar vortices to the side layers (see Pothérat *et al.* (2000)).

The case $Ha = 1822.2$, with a second steady state featuring reconnected vortices, stands slightly apart: the curve $Re_b(Re^o)$ indeed first follows scaling (33) over a short interval, then shifts away

from it as the first instability appears. At high Re^0 , it slowly converges toward (34), well inside the second unsteady regime.

The effect of the side walls is particularly visible when comparing graphs obtained for different injection scales. While the relation between Re^b and Re^0 closely follows the same pattern in both cases, the constant C_0 in scaling (16) is a little smaller for $\lambda_i = 0.3$ than for $\lambda_i = 0.1$ ($C_0 \simeq 0.18$ vs. $C_0 \simeq 0.24$). Larger vortices are indeed more sensitive to friction from the side walls because a larger proportion of the lattice is in direct contact with them. Furthermore, the values of Re^0 reached in the experiment for $\lambda_i = 0.3$ are not large enough for the average flow to reach a fully developed inertial regime.

It seems nevertheless that, at least at $Ha = 1093.3$ and $Ha = 1822.2$, Re^b varies as $Re^b \simeq 0.021Re^0$, which would suggest that in the early stages of the unsteady regime, viscous effects are still the main source of three-dimensionality in the large structures of the average flow.

For $\lambda_i = 0.1$, velocity fluctuations U'_b just outside the bottom Hartmann layer follow a unique law of the form $Re^{b'} \simeq C'_b \lambda_i (Re^0)^{2/3} Ha^{1/3}$, with $C'_b \simeq 1.05$, in the limit $Re^0 \rightarrow \infty$. This law is satisfied to a remarkable precision as soon as the flow is sufficiently turbulent (see figure 8, top). The scaling in $\lambda_i Ha^{1/3}$ reflects an increase with λ_i and Ha in the intensity of velocity fluctuations relative to the mean flow (*i.e.* $U'_b/U_b \sim \lambda_i Ha^{1/3}$). For a given value of Re^0 , turbulent structures indeed become more and more two dimensional when Ha is increased, and all the more so as they are large (hence the positive exponent of λ_i). Energy transfer from the main flow to them and through them to smaller scales is then progressively opposed by friction in the Hartmann layer (which incurs a dissipation of the order of $-Ha\rho\nu U_b'^2/l_\perp^2$, on a structure of size l_\perp), rather than by Joule dissipation in the bulk of the flow (of the order of $-Ha^2\rho\nu U_b'^2/l_\perp^2$). This phenomenon was recently observed in high precision simulations of the flow in a duct past a cylinder wake by Kanaris *et al.* (2013). Once it is factored in, it remains that $Re^{b'} \sim (Re^0)^{2/3}$, which is of the form of (19), and therefore indicates that not only fluctuating structures are three-dimensional but also that their three-dimensionality is entirely driven by inertial effects.

The variations of $Re^{b'}$ for $\lambda_i = 0.3$ (figure 8, bottom) confirm this tendency as for $Ha \geq 3644.3$, $Re^{b'}$ follows practically the same law as for $\lambda_i = 0.1$, albeit with a slightly lower value of constant C'_b (0.85, vs. 1.05). As for the average flow, this difference can be attributed to the greater influence of the side walls at higher λ_i . Even for the lowest available value of $Ha = 1093.3$, the inertial regime is well established, although the asymptotic law stands a little lower than for higher Ha ($C'_b = 0.67$). This value of C'_b reflects a non asymptotic behaviour. The scaling $U'_b/U_b \sim \lambda_i Ha^{1/3}$ can indeed only be expected to be valid in the limit $Ha \rightarrow \infty$ but not in the limit $Ha \rightarrow 0$, where non-MHD turbulence would still feed strong fluctuations.

5.2 Influence of the upper Hartmann wall

Now that regimes of quasi-two dimensionality, inertialess three dimensionality and purely inertial three dimensionality are identified, we shall examine the flow in the vicinity of the upper Hartmann wall to determine its influence on the flow dynamics within these regimes. In particular, we shall seek the conditions in which the current injected at the bottom Hartmann wall feeds into the Hartmann layers near the the top walls (when $l_z \gtrsim h$ and $l_z \gg h$ according to the theory from section 2.5).

The variations of Re^t , built on the average flow near the top wall, with Re^0 are shown in figure 9 for $\lambda_i = 0.1$ and $\lambda_i = 0.3$. Their general aspect is somewhat similar to those of Re^b with Re^0 (figure 7), with a linear relation in the inertialess regime (for $Re^0 < Re_I^0$), and a scaling of the form $Re^t \sim (Re^0)^{2/3}$ in the purely inertial regime (for Re^0 sufficiently larger than Re_I^0). There are, however, two major differences. Firstly, in the inertialess regime, a dependence on Ha of the form (22) is present (with $C_t^0 = 0.22$ vs. $C_b^0 = 0.24$ for $\lambda_i = 0.1$, and $C_t^0 = 0.18 \simeq C_b^0$ for $\lambda_i = 0.3$). The

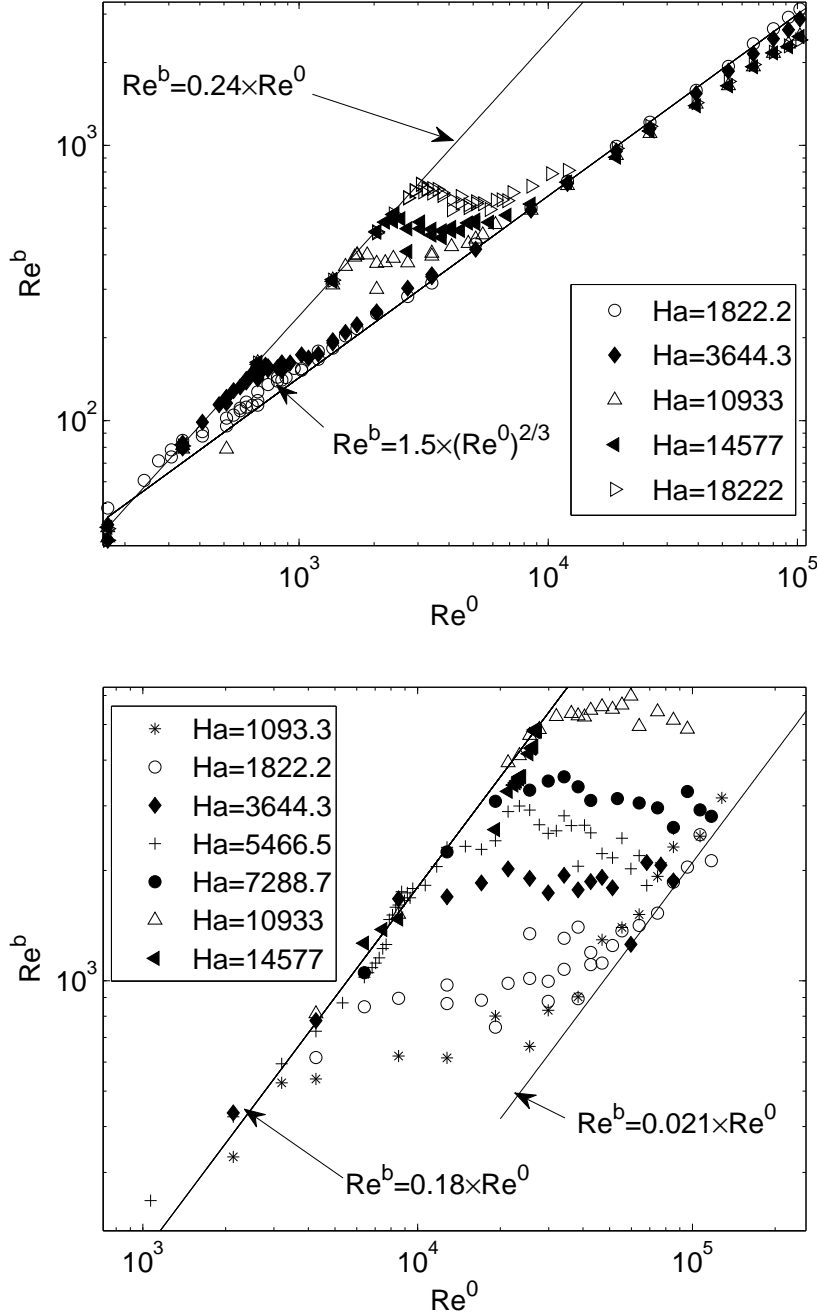


Figure 7: Graphs of Re^b vs. Re^0 representing the average flow near the bottom wall for measurements spanning the whole range of parameters accessible in the experiment (see figures 4 to 6), for $\lambda_i = 0.1$ (top) and $\lambda_i = 0.3$ (bottom). Scaling laws for the inertialess regime (of the form (16)) and purely inertial regime (19) are represented by solid lines.

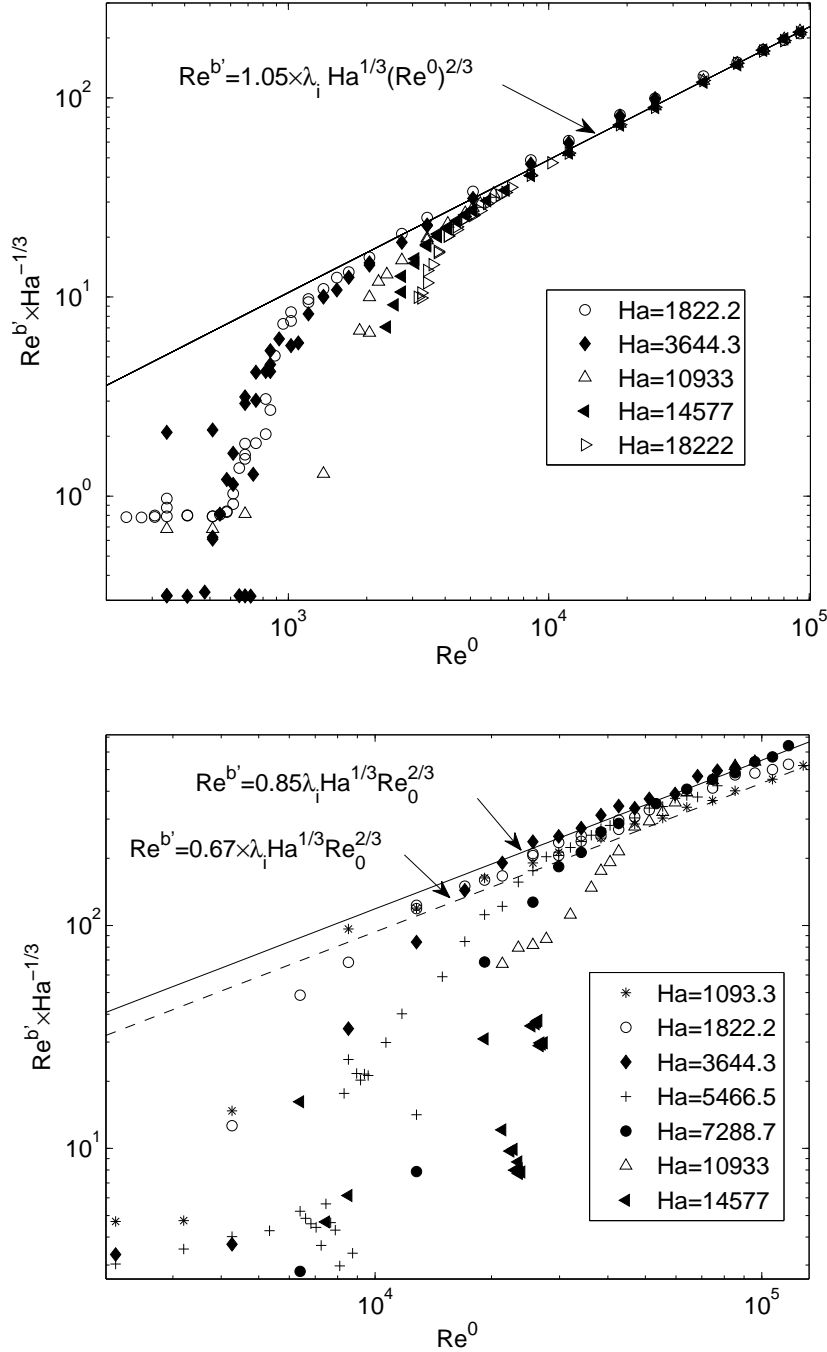


Figure 8: Graphs of $Re^b Ha^{-1/3}$ vs. Re^0 , representing the RMS of velocity fluctuations near the bottom wall for measurements spanning the whole range of parameters accessible in the experiment, for $\lambda_i = 0.1$ (top) and $\lambda_i = 0.3$ (bottom). Scaling laws for the purely inertial regime (19) are represented by solid and dashed lines.

graph for $\lambda_i = 0.3$ was scaled to find an estimate for the second constant in (22), $D_t^{(Ha)} \simeq 3.10^3$. Since average flow patterns at $Ha > 7500$ were found identical on both Hartmann walls, the fact that flows intensities are also close at high Ha is an early indication that the average flow is quasi-two dimensional in the limit $Ha \rightarrow \infty$. For lower Ha , on the other hand, the validity of (22) indicates that the average flow loses intensity away from the bottom plate under the effect of viscous friction. The second important difference between the variations of Re^t and Re^b is visible on the graph for $\lambda_i = 0.1$: in the inertial regime too, Re^t depends on Ha , but this time according to scaling (24). This not only confirms the finding of section 5.1, that three-dimensionality is driven by inertial effects, but also and most importantly, together with the validity of (22) in the range of lower Re^0 , it suggests that the upper wall actively influences the flow according to the mechanism identified in section 2.5, where part of the current injected near the bottom wall was concentrated in the top Hartmann layer. For $\lambda_i = 0.3$, on the other hand, the purely inertial asymptotic regime was not reached in the average flow, as already suggested by the variations of Re^b in section 5.1.

As for the average flow, the variations of the intensity of flow fluctuations near the top plate with Re^0 , reported in figure 10, resemble those near the bottom wall but exhibit a non-asymptotic behaviour at low Ha . In the limit of large Ha , $Re^{t'}$ tends towards a law of the form, $Re^{t'} \simeq C'_t \lambda_i (Re^0)^{2/3} Ha^{1/3}$, which only differs from $Re^{b'}$ through $C'_t = 0.88$, which is slightly lower than $C'_b = 1.05$. The scaling exponent for Re^0 itself confirms the presence of three-dimensionality driven by inertial effects, which was already visible in the variations of $Re^{b'}(Re^0)$ in section 5.1. The most remarkable point is that unlike for the base flow, the scaling exponent of Re^0 in the law $Re^{t'}(Re^0)$ is different at low Ha than in the limit of high Ha . At low Ha , it is of the form $Re^t \simeq C'_t(Ha) \lambda_i Ha^{1/3} (Re^0)^{1/2}$. This phenomenon is clearly identifiable over one to two decades of Re^0 at $\lambda_i = 0.1$ for $Ha \leq 3644.3$, and also at $\lambda_i = 0.3$ for $Ha < 1822.2$. The corresponding flow fluctuations are of much lower intensity than predicted by any of the scenarii of section 2.5 involving an active influence of the top wall on the flow, so one can infer that the electrically driven flow does not reach the upper wall (*i.e.* $l_z^{(N)} < h$). Instead, the exponent 1/2 of Re^b in the non asymptotic law matches that found by Duran-Matute *et al.* (2010) in a non-MHD inertial regime. It can be understood as follows: for the lowest values of Ha , the flow near the bottom wall is still entrained as predicted in section 2 over a height $l_z^{(N)} < h$ (given by (17)) and so the scaling law (16) for Re^b still holds. Fluctuations, by contrast, are not directly driven by current injection but receive energy from the average flow by inertial transfer. Furthermore, the non-asymptotic behaviour of $Re^{b'}$, visible at low Ha in figure 8 (bottom), suggests that for such structures, the core current becomes comparable to the current through the bottom Hartmann layer (this electric "leak" from the bottom Hartmann layer explains the lower intensity of the fluctuations). In this case the fluctuations are powered by inertial transfer over the whole fluid layer of height $l_z^{(N)}$ where current passes. The Lorentz force balances inertia there, and is of order $\sigma B^2 U_c$, as in the non-MHD inertial regime identified by Duran-Matute *et al.* (2010) (see the end of section 5.1) and this translates into a fluctuating velocity in the core U'_c scaling as $(Re^0)^{1/2}$. The flow near the top plate is thus not connected to this layer by eddy currents. Instead, it is entrained by viscous friction through the top fluid layer of thickness $h - l_z^{(N)}$. U_t is therefore proportional to U'_c and decreases with $h - l_z^{(N)}$. This explains that $Re^{t'} \sim (Re^0)^{1/2}$ and, since $l_z^{(N)}$ increases with Ha , it also explains that at low Ha , velocity fluctuations decrease faster when Ha decreases, than their scaling as $Ha^{1/3}$ at high Ha .

A remark must be made here on the validity of the velocity measurements near the top wall in such a strongly three-dimensional flow. Near the top Hartmann walls, the current density in the core is no smaller than that in the top Hartmann layer and so (32) becomes inaccurate. The quantity $B \langle \|\nabla \phi_t\| \rangle_t$ may still be interpreted as a velocity but rather represents an average over the top layer of thickness $h - l_z^{(N)}$ than the velocity in the vicinity of the top Hartmann layer.

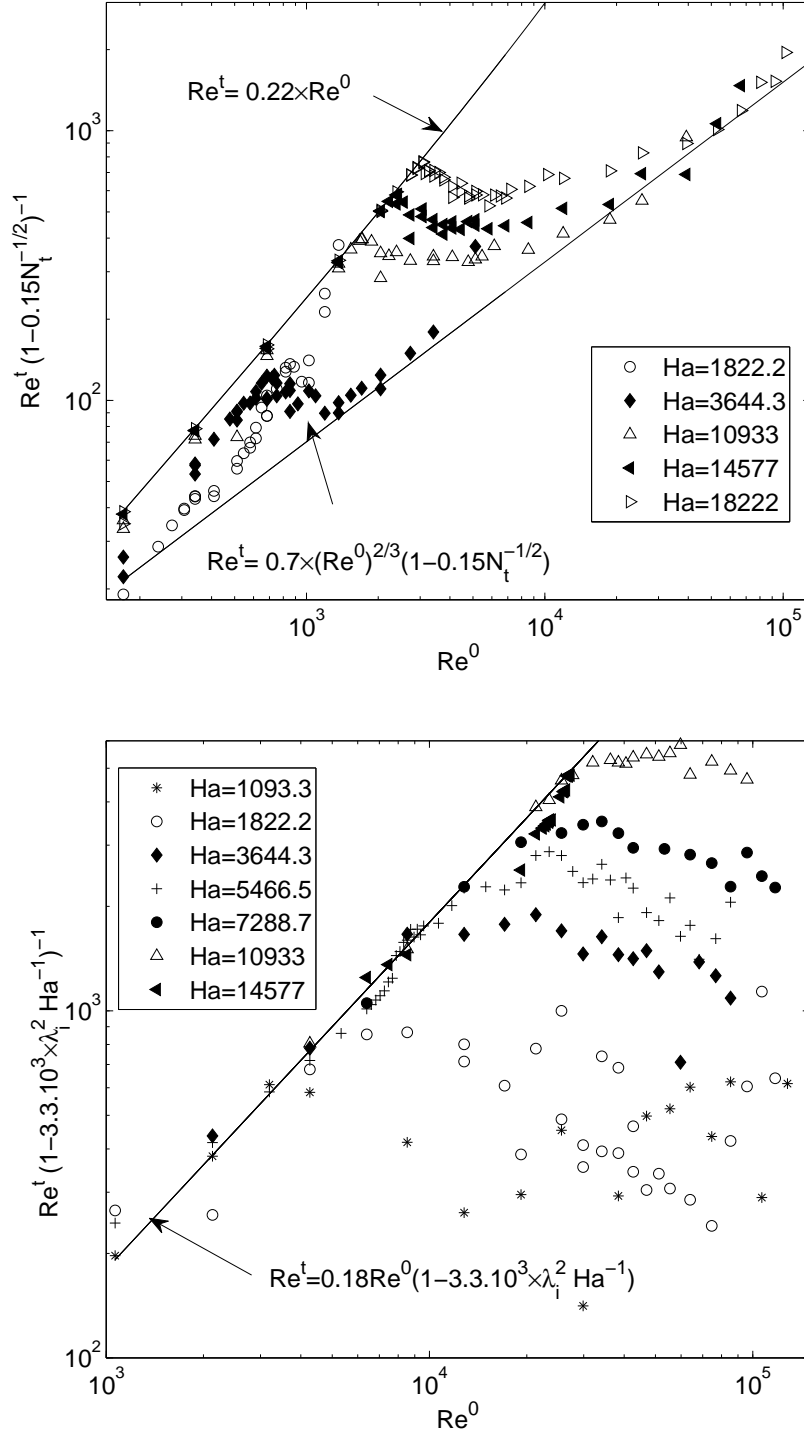


Figure 9: Graphs of Re^t vs. Re^0 , for measurements spanning the whole range of parameters accessible in the experiment, for $\lambda_i = 0.1$ (top) and $\lambda_i = 0.3$ (bottom). Top: curves are scaled by $(1 - 0.15 \times N_t^{-1/2})^{-1}$ to show that all curves collapse into a scaling of the form (24) in the high Re^0 range. A similar collapse happens at low Re^0 for scaling (22) (not represented here for concision). Bottom: curves are scaled by $(1 - 3.3 \cdot 10^3 \times \lambda_i^2 Ha^{-1})^{-1}$ to show that all curves collapse into a scaling of the form (22). Values of Re^0 accessible in the experiment were not large enough to verify inertial scaling (24) at $\lambda_i = 0.3$.

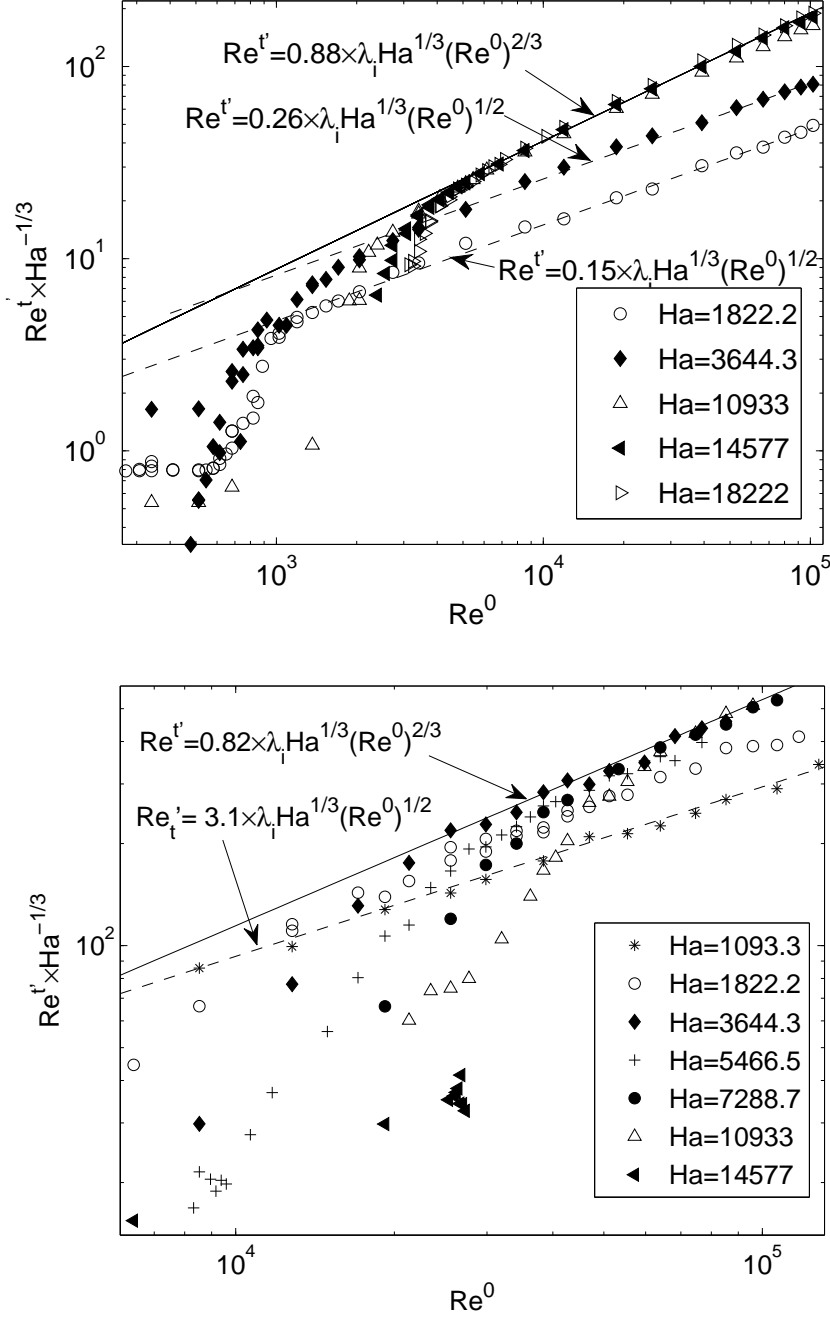


Figure 10: Graphs of $Re^t Ha^{-1/3}$ vs. Re^0 , for measurements spanning the whole range of parameters accessible in the experiment, for $\lambda_i = 0.1$ (top) and $\lambda_i = 0.3$ (bottom). Scalings laws corresponding to the purely inertial regime are represented by solid lines when the top wall influences the flow ($l_z^{(N)} \gtrsim h$ or $l_z^{(N)} \gg h$, scaling (24)) and by dashed lines when they don't ($l_z^{(N)} < h$, scaling of the form (20)).

5.3 Symmetric and anti-symmetric three-dimensionalities in profiles along Shercliff walls

Unlike Hartmann layers, Shercliff layers, which develop along walls parallel to the magnetic field, do not possess a property providing a simple relation between electric potential at the wall ϕ_S and velocities in the core (such as (30)) and so there is no simple way to deduct velocity variations along \mathbf{B} from time-series of non-intrusive measurements of electric potential at the wall. Furthermore, Shercliff layers are intrinsically three-dimensional because they result from a balance between horizontal viscous friction and the Lorentz force, which, as in the mechanisms responsible for three-dimensionality in the core, draws a horizontal current from the core. Nevertheless, If three-dimensionality is present in the core, then the current drawn from it into the Shercliff layers depends on z . More specifically, the *asymmetric* three-dimensionality in the core described in section 2.6 translates into antisymmetric component of the profile of $\phi_S(z)$ of order at least z^3 (A z -linear antisymmetric component of $\phi_S(z)$, by contrast, corresponds to constant and therefore non-divergent vertical current. Such a current can only be fed by the top and bottom Hartmann layers, which connect to the Shercliff layers at the top and bottom edges of the vessel, not from the core). Similarly, *Symmetric* three-dimensionality in the core leads to a symmetric deformation of $\phi_S(z)$. The reverse, however isn't true, since even in quasi-two dimensional flows, intrinsic three-dimensionality within the Shercliff layers induce a symmetric three-dimensional component in $\phi_S(z)$ (see for example, Moreau (1990)). Nevertheless, Since this deformation is driven by linear viscous friction, it must depend linearly on the flow intensity, as measured by U_b . Consequently, symmetric three-dimensionality can still be detected by tracking the deformation of the symmetric part of $\phi_S(z)/(BU_b L_i)$ and $\phi'_S(z)/(BU'_b L_i)$ with Re^0 . The distinction between symmetric and anti-symmetric three dimensionality is particularly important in the context of the present work, as anti-symmetric three-dimensionality gives a measure of the influence of the forcing on the flow dynamics, and of the non-universality associated to it.

Before we analyse the time-averaged and RMS fluctuations of $\phi_S(z)$ recorded along the Shercliff wall located at $x = 0$ in the light of these remarks, a word of caution must be given to the reader as unfortunately, signals recorded along Shercliff walls cannot achieve as high a level of quality as those recorded along Hartmann walls. Since walls are electrically insulating and all electrodes are located a distance much larger than $h/Ha^{1/2}$ from them, the current density there is significantly weaker and so are the recorded signals. Consequently, our analysis will be restricted to the turbulent regimes, where the flow and the signals are more intense. Profiles are chosen at $(x/L, y/L) = (0, 0.24)$ and for $\lambda_i = 0.1$ only, but are representative of the phenomenology observed in other cases.

Figure 11 shows the profiles of $\langle \phi_S(z/h) - \phi_S(1/2) \rangle$ and $\langle \phi_S(z/h)^2 \rangle^{1/2} - \langle \phi_S(1/2)^2 \rangle^{1/2}$ for the same set of values of Re^0 , at different Ha . They are respectively normalised by $BU_b L_i$ and $BU'_b L_i$. Firstly, the amplitude of the variations of both these quantities decreases by about an order of magnitude between $Ha = 1822.2$ and $Ha = 18222$: this simply reflects that the flow becomes closer to quasi-two dimensionality as Ha increases and that the relative amount of current that transits from the core to the Shercliff layers reduces correspondingly. Secondly, all graphs show that the vertical gradient of these quantities increases with Re^0 . This is due to the increasing amount of current drawn into the core by inertial effects, which loops back through the Shercliff layers. This effect being non-linear, it can be measured on the graphs at the discrepancy between curves at different values of Re^0 . In this respect, at $Ha = 1822.2$, the eddy currents originating from the core are strongly concentrated near the bottom wall and practically zero near the top wall (this is even more spectacular on the profiles of fluctuations). Together with the scaling $Re'_t \sim (Re^0)^{1/2}$ observed in this regime (section 5.2), this concurs to show that the top wall is not active and that $l_z^{(N)} < h$. The phenomenology is similar at $Ha = 3644.3$, except for a slight gradient in the

vicinity of the top wall, suggesting that $l_z^{(N)}$ is closer to h and that eddy currents already appear between the core and the top Hartmann layer. At the two highest values of Ha , the profiles of both averages and fluctuations become more symmetric, to be almost symmetric at $Ha = 18222$, but with an important difference between them. All average profile converge towards a single curve at high Re^0 : this indicates linearity with the flow intensity and therefore suggests that the three-dimensionality corresponding to this vertical current is due to the viscous effects in the Shercliff layers. By contrast, the profiles of fluctuations are more dispersed: although the amplitude of the corresponding currents are quite weak, this non-linearity suggests the presence of symmetric three-dimensionality, as theorised in section 2.6.

Symmetric three-dimensionality can be more precisely traced by inspecting the symmetric part of the profiles of $\langle \phi_S(z/h) - \phi_S(1/2) \rangle$ and $\langle \phi_S(z/h)^2 \rangle^{1/2} - \langle \phi_S(1/2)^2 \rangle^{1/2}$, on figure 12. While inertia-driven, symmetric three-dimensionality is practically absent from fluctuations at low Ha , it becomes dominant a large Ha . The average flow, by contrast, exhibits the opposite behaviour, with inertia-driven symmetric three-dimensionality absent a high Hartmann. Since the profiles of fluctuations are highly symmetric in this regime, this important difference shows that at $Ha > 10933$, where τ_{2D} becomes shorter than the turnover time for the large scales, asymmetry induced by the forcing is mostly confined to the base flow and the Lorentz force damps it out before it is transferred to turbulent fluctuations. The dimensionality of turbulent fluctuations generated in this regime is therefore subject to little influence from the inhomogeneity of the forcing.

Finally, the antisymmetric part of the profiles of $\langle \phi_S(z/h) - \phi_S(1/2) \rangle$ and $\langle \phi_S(z/h)^2 \rangle^{1/2} - \langle \phi_S(1/2)^2 \rangle^{1/2}$ carry information about the lengthscale of momentum diffusion by the Lorentz force $l_z^{(N)}(B, U_b)$, defined by (17). Profiles against $z - h/2$ normalised by this lengthscale (*resp.* $l_z'^{(N)} = l_z^{(N)}(B, U_b')$) built on average (*resp.* fluctuating) quantities are gathered on figure 13, left (*resp.* right). With this choice of variables, since $l_z^{(N)}$ and $l_z'^{(N)}$ decrease with Ha , curves obtained at lower Ha are shorter than those at high Ha , and all curves are centred on 0. Profiles of average and fluctuations respectively collapse well a single curve, thus confirming the validity of scaling (17) for the diffusion lengths $l_z^{(N)}$ and $l_z'^{(N)}$, respectively for the average flow and the fluctuations. The average potentials follow a linear profile $\phi_S(z/l_z^{(N)})$, with strong discrepancies to it in regions where $|(z - h/2)/l_z^{(N)}| > 0.5$ (marked by horizontal dashed lines). Only at $Ha = 1822.2$ are these regions clearly reached, as $l_z^{(N)}$ is notably smaller than h whereas at $Ha = 3644.3$, $l_z \simeq h$, depending on Re^0 . The regions where $|(z - h/2)/l_z^{(N)}| > 0.5$ are the races in the antisymmetric profile of the near bottom wall region where strong current is present in the core and of the region $l_z^{(N)} < z < h$ situated beyond the diffusion length $l_z^{(N)}$. For $|(z - h/2)/l_z^{(N)}| < 0.5$, by contrast, momentum diffusion by the Lorentz force dominates inertia: the current in the core collapses and so does therefore the return vertical current in the Shercliff layers. For $Ha > 3644.3$, $l_z^{(N)} < h$: discrepancies to linearity are less pronounced and reflect eddy currents more homogeneously spread along the height of the vessel. This phenomenology holds for both the average flow and the fluctuations but the collapse to a single curve is significantly better on the profiles of fluctuations. Most remarkably, the antisymmetric part of the profile of fluctuations is practically 0 in the region $|(z - h/2)/l_z^{(N)}| < 0.5$. Turbulence in this region is therefore not affected by the asymmetry of the forcing. For $Ha > 10933$, this extends along the full height of the vessel. Together with the presence of symmetric three-dimensionality in the symmetric part of the profile, this establishes that the three-dimensionality of turbulence observed in this range of parameters is not induced by the forcing, even though the latter may still induce some three-dimensionality in the base flow.

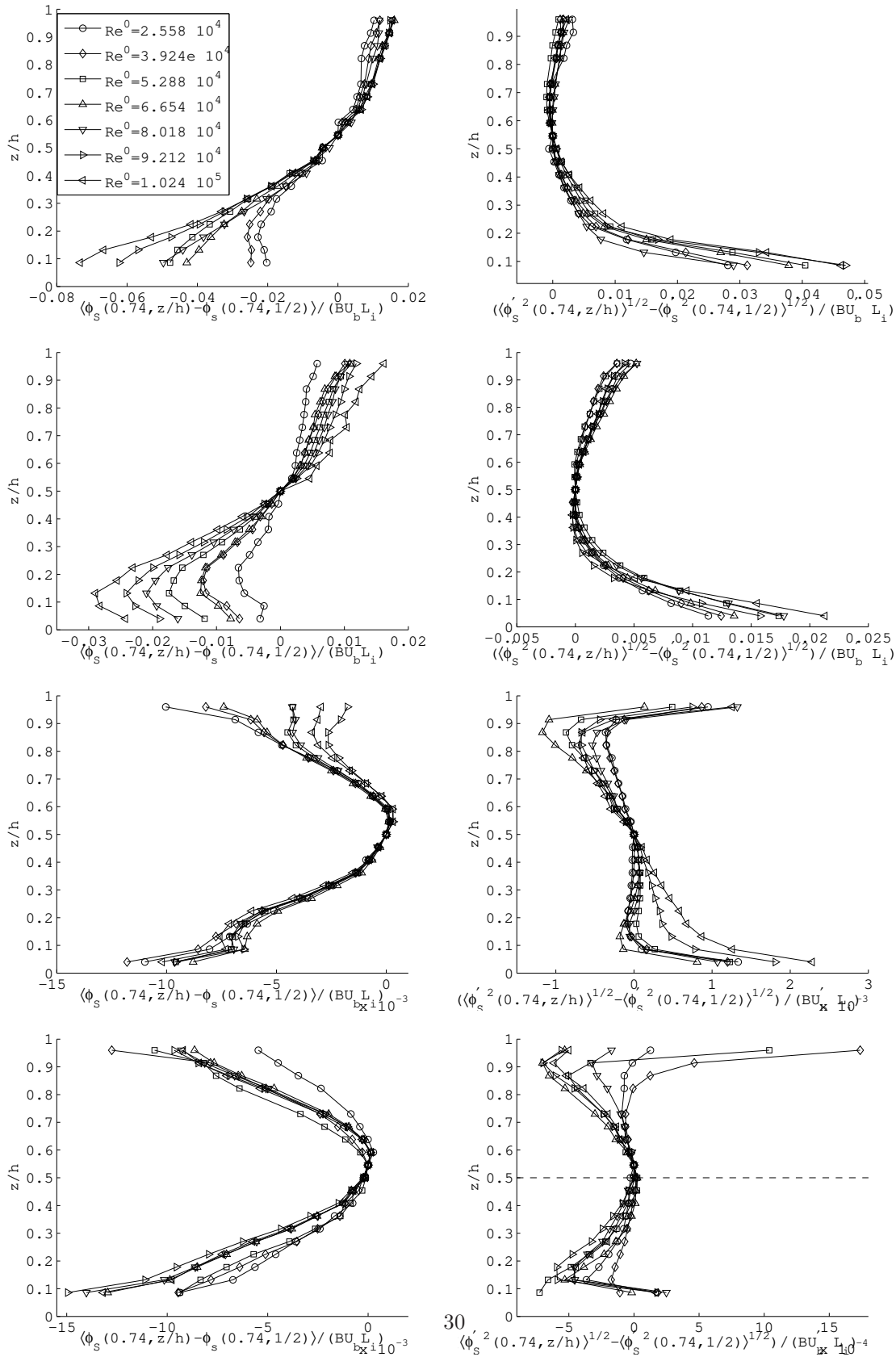


Figure 11: Profiles of $\langle \phi_S(z/h) - \phi_S(z/h = 1/2) \rangle$ (left), and $\langle \phi_S'(z/h)^2 \rangle^{1/2} - \langle \phi_S'(z/h = 1/2)^2 \rangle^{1/2}$ (right) measured at $(x, y)/L = (0, 0.24)$. From top to bottom: $Ha = 1822.2, 3644.3, 10933, 18222$.

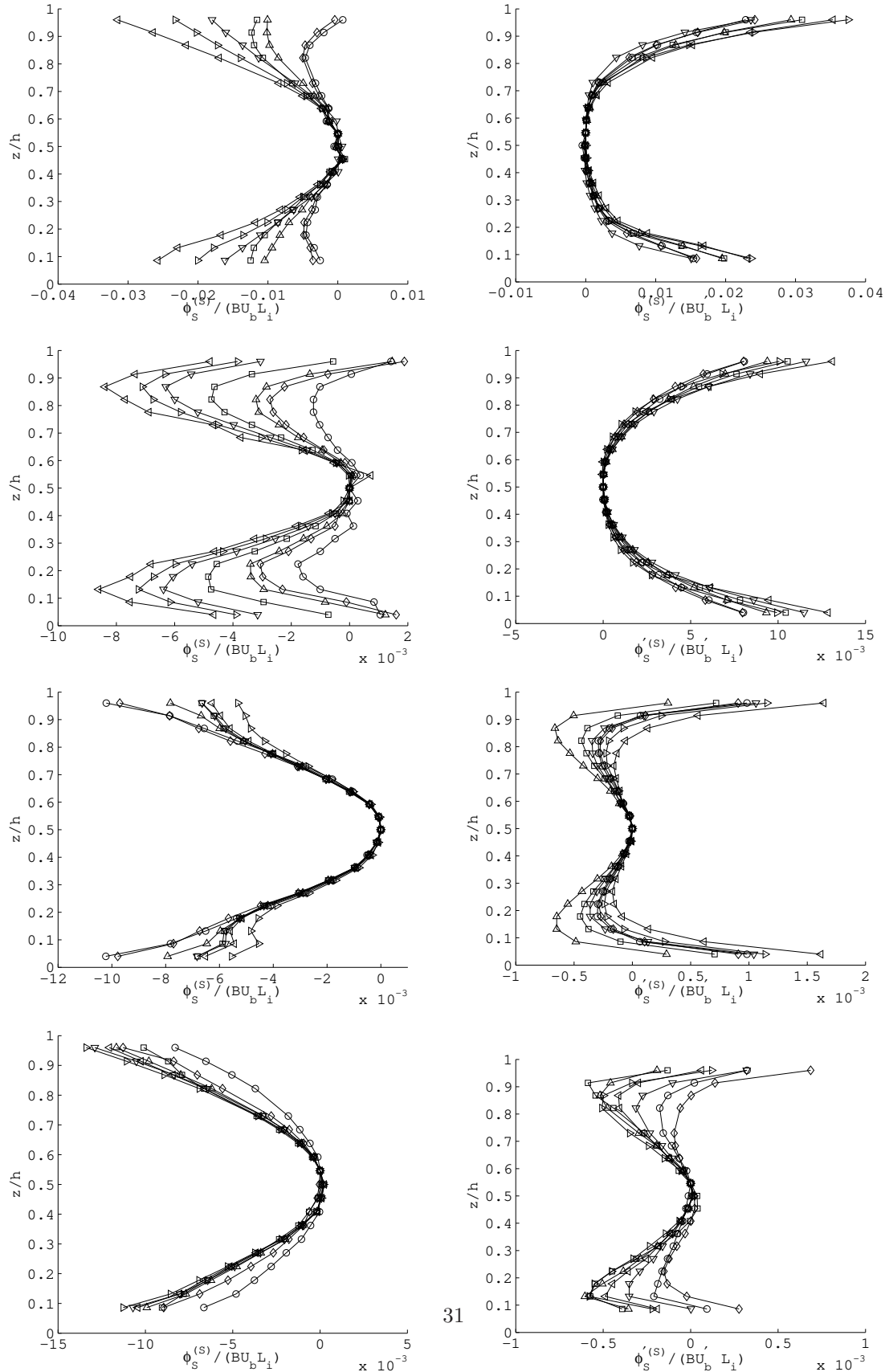


Figure 12: Symmetric part (superscript (S)) of $\langle \phi_S(z/h) - \phi_S(z/h = 1/2) \rangle$ (left), and of $\langle \phi_S(z/h)^2 \rangle^{1/2} - \langle \phi_S(z/h = 1/2) \rangle^{1/2}$ (right), measured at $(x.u)/L = (0, 0.24)$. From top to bottom:

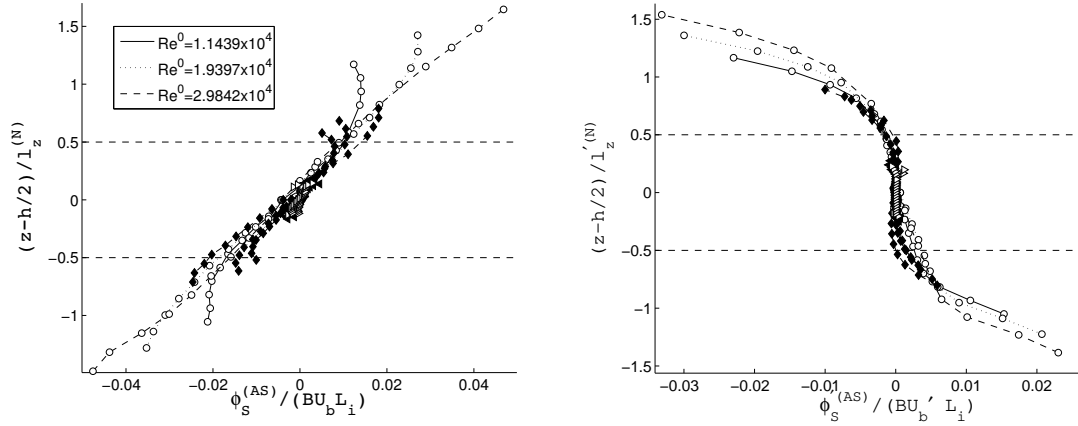


Figure 13: Antisymmetric part (superscript (AS)) of the profiles of $\langle \phi_S(z/h) - \phi_S(1/2) \rangle$ (left) and $\langle \phi_S'(z/h)^2 \rangle^{1/2} - \langle \phi_S'(z/h = 1/2) \rangle^{1/2}$ (right), measured at $(x/L, y/L) = (0, 0.24)$, with z respectively normalised by $l_z^{(N)}$ and $l_z'^{(N)}$ (built on U_b and U_b'). Profiles are plotted for $\lambda_i = 0.1$, for 5 values of Ha (marked by the same symbols as in figure 7), and 3 values of Re^0 for each value of Ha .

6 Weak vs. Strong three-dimensionalities in unsteady regimes

6.1 Global quantification of *weak* and *strong* three-dimensionality

In sections 2 and 5, the vertical profiles of electric potential and the scalings for U_b , U_t , U_b' and U_t' were shown both to be efficient tools to detect three-dimensionality, and to contain a signature of its origin, either inertial or viscous. They were shown to characterise the influence of bottom and top Hartmann wall separately too. This global approach, however, provides little information on the nature of the three-dimensionality involved, and although the quantity of current drawn into the core by three-dimensional mechanisms can be inferred from these scalings, a measure of three-dimensionality itself is still missing. To address these closely related questions, we shall start by quantifying weak and strong three-dimensionalities, which we previously introduced in Klein & Pothérat (2010), and which were visible from flow visualisations in section 4. In particular, we shall estimate the extent in which either form of three-dimensionality is eradicated in the quasi-two dimensional limit.

Let us start by recalling that *weak* three-dimensionality is characterised by a variation in flow intensity between two-dimensional "slices" of topologically equivalent flows in the (x, y) plane. *Strong* three-dimensionality, by contrast, involves different profiles of physical quantities along z at different locations (x, y) . Following Klein & Pothérat (2010), their respective occurrence shall be quantified by comparing measurements at bottom and top Hartmann walls at $z = 0$ and $z = h$,

by means of two types of correlations:

$$C'_1 = \frac{\sum_{t=0}^T \partial_y \phi'_b(t) \partial_y \phi'_t(t)}{\sqrt{\sum_{t=0}^T \partial_y \phi'^2_b(t) \sum_{t=0}^T \partial_y \phi'^2_t(t)}} \quad (35)$$

$$C'_2 = \frac{\sum_{t=0}^T \partial_y \phi'_b(t) \partial_y \phi'_t(t)}{\sum_{t=0}^T \partial_y \phi'^2_b(t)}, \quad (36)$$

where T is the duration of the recorded signals. Values of C'_1 depart from unity whenever strong three-dimensionality is present, but is unaffected by weak three-dimensionality. C'_2 , on the other hand, differs from unity whenever either weak or strong three-dimensionality is present. In order to minimise the influence of the walls, we shall reason on the the spatial averages $\overline{C'_i}$ and $1 - \overline{C'_i}$ of C'_i and $1 - C'_i$ over the central square region (see 3). Whilst $1 - \overline{C'_1}$ and $1 - \overline{C'_2}$ give a measure of three-dimensionalities, $\overline{C'_1}$ and $\overline{C'_2}$ reflect the emergence of two-dimensionality, respectively in the strong sense, and in both the weak and the strong sense. A minor limitation of this method, however, is that fluctuations that remain *at all time* symmetric with respect to the vessel mid-plane ($z/h = 1/2$) cannot be detected as they do not affect the values of C'_1 nor C'_2 . Fluctuations that are symmetric *on average* such as those detected in the antisymmetric part of ϕ'_S (section 5.3), may, by contrast affect the values of the correlations. While the former type of fluctuation is unlikely to generate strong three-dimensionality, the latter is the most likely form of *strong* symmetric three-dimensionality, since it results from randomly localised three-dimensional disturbances, which are unaffected by the asymmetry of the forcing and therefore distributed symmetrically along the vessel height.

$\overline{C'_i}$ and $1 - \overline{C'_i}$ are plotted in figure 14 against the true interaction parameter based on the velocity fluctuations and the injection scale $N'_t(L_i) = (\sigma B^2 L_i / \rho U'_b) \lambda_i^{-2}$. All our measurement points collapse into two single curves $\overline{C'_1}(N_t)$ and $\overline{C'_2}(N_t)$, indicating that the three-dimensionality in the fluctuations is exclusively of inertial nature. This is consistent with the fact that the scalings found for fluctuations U'_b and U'_t in section 5 were all explained by the presence of inertia in the core. In the limit $N_t \rightarrow \infty$, both types of correlations become close to 1 to a precision of about 1%. This confirms that in these regimes, the flow is very close to quasi-two dimensionality. Furthermore, in the limit $N_t \rightarrow \infty$, $1 - \overline{C'_1}(N_t) \sim N_t^{-0.9}$, and $1 - \overline{C'_2}(N_t) \sim N_t^{-0.9}$, until these quantities reach a plateau that corresponds to the level of signal noise. In fact two such plateaux shoot off from the main $N_t^{-0.9}$ law, that correspond to the two different levels of signal to noise ratio for $\lambda_i = 0.1$ and $\lambda_i = 0.3$. Nevertheless, this asymptotic behaviour gives a strong experimental evidence that the flow becomes *asymptotically* quasi-two dimensional and that a vanishingly small amount of three-dimensionality always remains present. By contrast, the transition between two and three dimensional states in MHD flows with non-dissipative boundaries (such as free-slip conditions studied by Thess & Zikanov (2007) or periodic boundary conditions by Zikanov & Thess (1998); Pothérat & Dymkou (2010)) occurred through bifurcations at a critical value of the parameter representing the flow intensity. This fundamental difference in behaviour must be attributed to the role of walls. This is consistent with the recent theory by Pothérat (2012) showing that the presence of walls maintains weak three-dimensionality so long as N is finite.

In the limit $N_t \rightarrow 0$, $\overline{C'_1}$ and $\overline{C'_2}$ exhibit several noticeable differences. Firstly, weak three-dimensionality appears significantly earlier (in the sense of increasing N_t) than strong three-dimensionality, since $\overline{C'_1} \sim N_t^{-1/2}$, whereas $\overline{C'_2} \sim N_t^{-1}$. This effect is in part due to the nature of the forcing: for low magnetic fields and strong currents, electric currents remain in the vicinity of

the bottom wall, where the flow is intensely stirred. By contrast, very little current flows near the top wall. Whatever weak flow remains there is mostly entrained by viscous and electromagnetic momentum diffusion from the intense flow near the bottom wall. Both share the same large patterns, as on the snapshots of streamlines (a) and (b) from figure 14, and are therefore somewhat correlated in the weak sense, even though the very small intensity of the flow near the top wall extinguishes correlation in the strong sense.

The power laws found in the limits $N_t \rightarrow 0$ and $N_t \rightarrow \infty$ intersect at $N_t = N_t^{2D} \simeq 4.5$, and remain remarkably valid in their respective ranges $N_t < 4.5$ and $N_t > 4.5$. In this sense, the value N_t^{2D} marks a form transition between quasi-2D and 3D states. We insist, however, that this isn't a critical value of N_t since no bifurcation occurs in the flow states at this point. Also, it provides a rather global appraisal of the flow state but it would be incorrect to assert that for $N_t > 4.5$, the flow is quasi-2D in the sense that every structure in the flow is.

6.2 Frequency dependence of weak and strong three-dimensionalities

We shall now seek to characterise three-dimensionality locally by analysing the frequency spectra from the fluctuations of $\nabla\phi$ near each of the Hartmann walls. On figure 14, pairs of such spectra are shown that were obtained from signals acquired at locations of either Hartmann walls exactly aligned with the magnetic field lines (*i.e.*, respectively at $z = 0$ and $z = h$, but at the same coordinates (x, y)). These were taken in the central square region, so as to minimise the influence of the side walls. For values of N_t noticeably higher than 4.5, the two spectra are practically identical, as would be expected of a flow that would be quasi-two dimensional at all scales. Since spectra do not carry any phase information, however, identical spectra do not provide a proof that all scales are indeed two-dimensional, but merely that no obvious three-dimensionality is present at any scale. Pairs of spectra at lower values of N_t , on the other hand, show a clear manifestation of three-dimensionality as fluctuations of higher frequency carry significantly less energy in the vicinity of the top wall than near the bottom wall. Fluctuations of lower frequency, by contrast, carry the same amount of energy. When N_t is reduced, the range of frequencies affected by three-dimensionality widens to the low frequency range and ends up contaminating the whole spectrum at the lowest values of N_t . This qualitative comparison of spectra indicates that fluctuations of higher frequencies, and smaller scales by extension, are more sensitive to three-dimensionality than those of lower frequencies and larger scales, in accordance with Sommeria & Moreau (1982)'s prediction. A closer inspection of superimposed spectra further suggests the existence of a cutoff scale f_c separating three-dimensional high frequency fluctuations from lower frequency fluctuations with the same amount of energy near both walls. It also appears that f_c increases with N_t . To quantify the behaviour of $f_c(N_t)$, we define a partial correlation function between signals on the bottom and top Hartmann walls in the strong sense:

$$c'_1(f) = \frac{\sum_{t=0}^T \mathcal{B}_f \partial_y \phi'_b(t) \partial_y \phi'_t(t)}{\sqrt{\sum_{t=0}^T \mathcal{B}_f \partial_y \phi'^2_b(t) \sum_{t=0}^T \partial_y \phi'^2_t(t)}} \quad (37)$$

The definition of $c'_1(f)$ hardly differs from that of $C'_1(f)$, but for the fact that the full signal recorded from the bottom wall is replaced by a filtered counterpart, processed through an 8^{th} order low-pass filter of cutoff frequency f , incurring neither phase nor amplitude distortion. Figure 15 shows the typical variations of $c'_1(f)$ when f spans the whole part of the spectrum resolved in our measurements. Their most important feature is the presence of a maximum, which can be understood by considering two spectra obtained from top and bottom walls overlapping up to a frequency f_c . Increasing f from 0 for $f < f_c$ adds fluctuations to the bottom signal that are

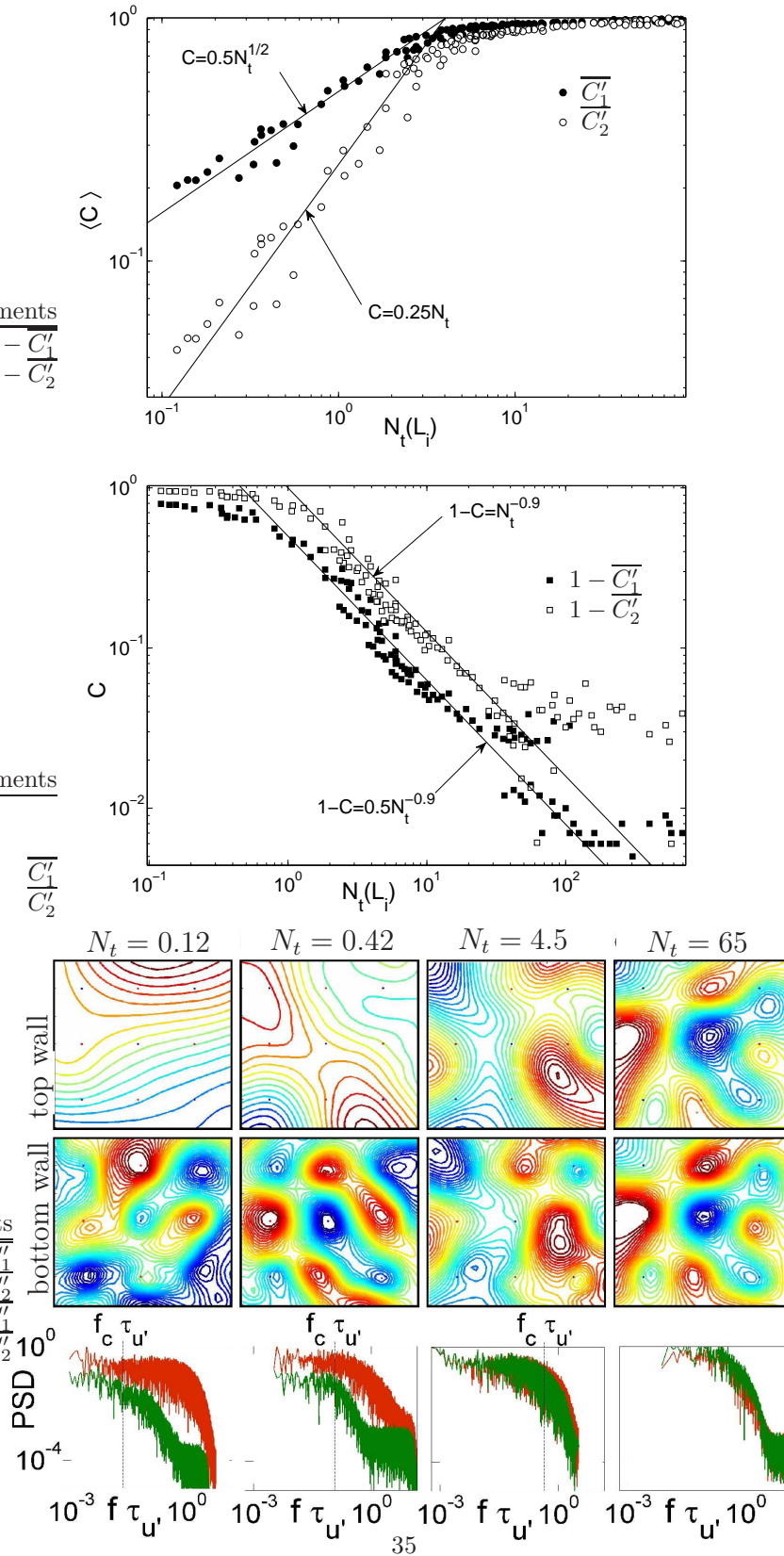


Figure 14: Correlations (top) and co-correlations (middle) of electric potential gradient between bottom and top Hartmann walls, averaged over the central square. Data were obtained both from measurements with $\lambda_i = 0.1$ and $\lambda_i = 0.3$. Bottom: snapshots of contours of electric potential taken for four values of N_t

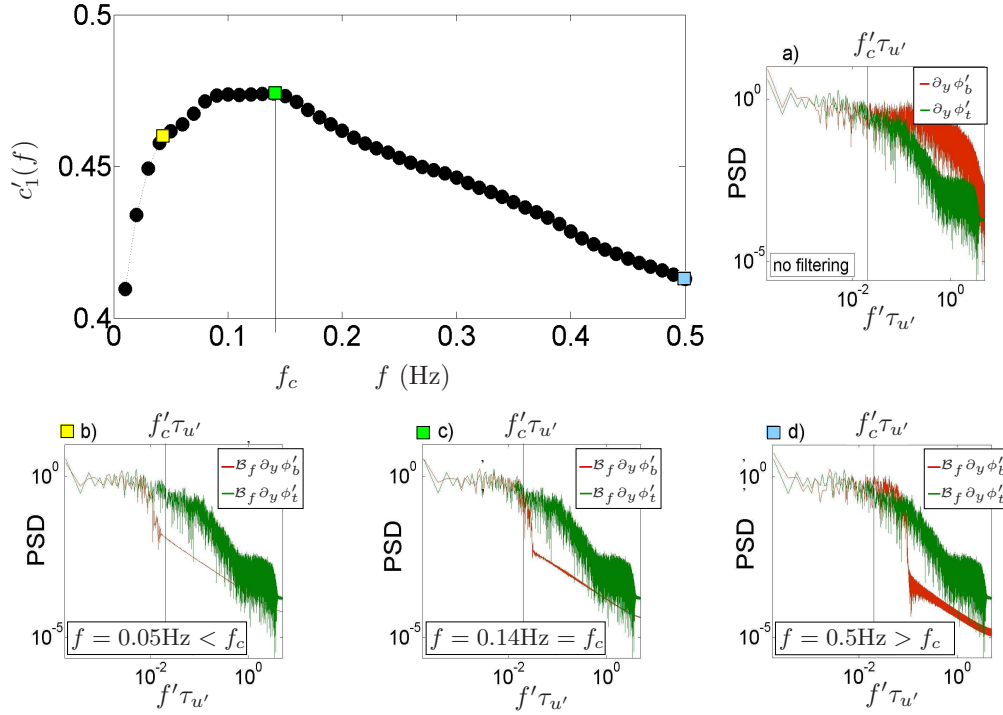


Figure 15: Variations of partial correlation $c'_1(f)$ with the cutoff frequency of the filter applied to the signal measured at the bottom wall. Curves are obtained for $\lambda_i = 0.1$ and $N_t = 0.12$ for a pair of probe within the central square. Curves obtained for different parameters exhibit the same features. Spectra of the filtered signals and top signals are shown below the graphs.

correlated with existing frequencies in the signal from the top wall, so $c'_1(f)$ increases. When f is increased beyond f_c , the fluctuations added to the bottom signal are uncorrelated from existing frequencies in the top one, so $c'_1(f)$ decreases. The position of the maximum thus gives a good measure of f_c . Note that the same approach cannot be applied to C'_2 , as a partial correlation $c_2(f)'$ obtained from C'_2 by replacing the bottom signal by a filtered counterpart would diverge in the limit $f \rightarrow 0$ because the filtered bottom signal vanishes in this limit (This feature is absent from the behaviour of $c_1(f)'$ because signals are normalised by their intensity by construction). Nevertheless, both from Sommeria & Moreau (1982)'s theory and from the theory developed in section 2, the existence of a cutoff lengthscale separating quasi-two dimensional from three-dimensional structures stems from no assumption on the nature of inertial effects so it can be expected to exist both for weak and strong three-dimensionality. Yet, if instabilities occurred at the scale of individual structures, they would incur strong rather than weak three-dimensionality so in any case, f_c is linked to the minimum size of structures that are stable to three-dimensional perturbations. The question of the nature of the instabilities that can occur below this size remains to be clarified with dedicated analysis.

The variations of $f_c(N_t)$ are represented on figure 16. Measurements points across the whole range of unsteady flows reachable in the experiment once again collapse into a single curve, so f_c is determined by N_t , as $C'_1(f)$ and $C'_2(f)$ were, with a scaling law

$$f_c \simeq 1.7 \tau_{u'}^{-1} N_t^{0.67}. \quad (38)$$

While this law is verified to a great precision for $\lambda_i = 0.1$ (the exponent 0.67 is obtained to a

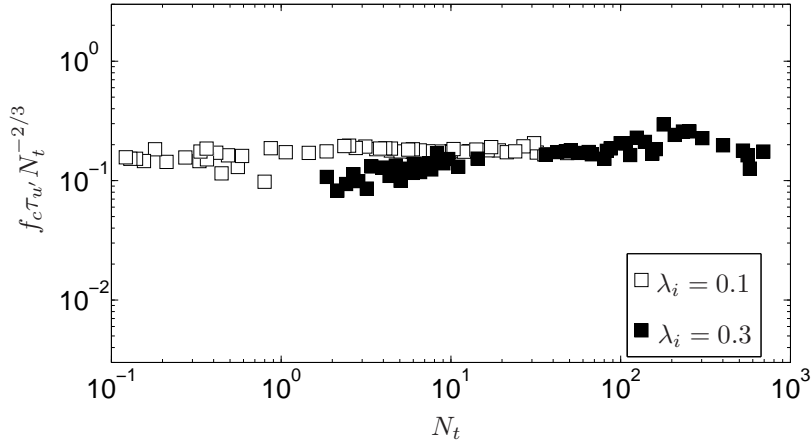


Figure 16: Cut-off frequency f_c , separating quasi two-dimensional fluctuations from three-dimensional ones, normalised by τ_u^{-1} , the eddy turnover frequency built on U_b' , vs. N_t .

precision of ± 0.03), a small departure to this law appears at low N_t for $\lambda_i = 0.3$, that must be attributed to the greater influence of the walls. Indeed the large vortices forced in such regimes can be expected to induce local separations of the parallel boundary layers, acting as a source of instability that could lower f_c . Unfortunately, our measurements do not allow us to test this hypothesis. It is however consistent with the fact that boundary layer separation is suppressed at higher N_t (see Pothérat *et al.* (2005)).

7 Conclusion

We have conducted a detailed analysis of the conditions of appearance of three-dimensionality in both in laminar and the turbulent regimes of a square array of electrically driven vortices. Three-dimensionality appears whenever viscous or inertial forces exist in the core of the flow, *i.e.* outside the Hartmann boundary layers. The nature of these forces could be identified through scaling laws linking the total current injected to drive the flow and the velocities in the vicinity of the bottom wall (where the flow is forced by injecting electric current), and the top wall. With the help of Reynolds numbers Re^b , Re^t , Re^0 representing these three quantities, these scaling bring a first answer to question (a) raised in introduction:

- Both quasi-two dimensional flows and flows where three-dimensionality is driven by viscous friction in the core obey scaling laws of the form first put forward by Sommeria (1988): $Re^b \sim Re^0$.
- For flows where three-dimensionality is driven by inertia, including turbulent ones, $Re^b \sim (Re^0)^{2/3}$.

Momentum diffusion along \mathbf{B} is opposed by either of these forces and this determines the thickness l_z of the fluid layer above the bottom wall where momentum diffuses. If viscous effects oppose the Lorentz force, then $l_z \sim l_\perp Ha$, whereas when inertia opposes it, $l_z \sim l_\perp N^{1/2}$. For a channel of height h , two regimes can be distinguished, that provide a quantitative answer to question (b) raised in introduction:

- If $h < l_z$, eddy currents flow in the top Hartmann layer and the upper wall is active in the sense that it strongly influences the flow. Re^t then scales either as $Re^t \sim Re^0(1 - D^{(Ha)}\lambda_i^2 Ha^{-1})$ in the inertialess regime, and as $Re^t \sim (Re^0)^{2/3}(1 - D^{(N)}N_t^{-1/2})$ in the inertial regime. The flow becomes quasi-two dimensional in the limit $l_z/h \rightarrow \infty$.
- If $h > l_z$, momentum diffusion doesn't reach the top wall and only a weak residual flow exists there. In the inertial regime, it follows the scaling found by Duran-Matute *et al.* (2010) of $Re^b \sim (Re^0)^{1/2}$.

These scalings were verified experimentally for two injection scales ($\lambda_i = 0.1$ and 0.3), $1093.3 \leq Ha \leq 18222$ and Re^0 up to 1.03×10^5 , which corresponded to a Reynolds number based on turbulent fluctuations $Re^{b'}$ of up to about 6×10^3 . Scaling laws corresponding to viscous effects were only clearly observed in the steady state or the average state of unsteady flows. By contrast, for flow fluctuations, inertia was the dominant force antagonising the Lorentz force. Turbulent regimes, in particular, were characterised by the true interaction parameter N_t alone, which represents the ratio of diffusion by the Lorentz force to inertia.

In these turbulent regimes, we were able to quantify *weak* and *strong* three-dimensionalities, which we first introduced in Klein & Poth erat (2010), both globally and in a scale-by-scale analysis of the flow. This brought further clarifications on the mechanisms driving three-dimensionality (question (a) and (c)):

- The transition between the quasi-two dimensional and three-dimensional states of wall-bounded MHD turbulence is a progressive phenomenon controlled by the true interaction parameter built on the large scales N_t . It doesn't occur at a bifurcation in the space of parameters, unlike in domains with slip-free boundaries only. Instabilities of individual structures are still most probably involved in *strong* three-dimensionality, but both *weak* and *strong* three-dimensionality only vanish in the limit $N_t \rightarrow \infty$, and not at a critical value of N_t .
- A cutoff scale exists in MHD turbulence, that separates quasi-two dimensional scales from three-dimensional ones, as predicted by Sommeria & Moreau (1982). Its existence could, however, only be confirmed experimentally for *strong* three-dimensionality, even though it is expected to be found for *weak* three-dimensionality too.

Finally, we tracked the trace of three-dimensionality due to the electric forcing by separating symmetric and antisymmetric parts of profiles of electric potential measured along Shercliff walls (question (d) raised in introduction). It turned out that when $\tau_{2D}(\lambda_i) \lesssim \tau_U(\lambda_i)$, the asymmetry between the top and bottom wall introduced by the forcing was dampened out during the energy transfer from the mean flow to the large turbulent scales. In this case, the trace of the forcing was mostly borne by the average flow. The features of the turbulence observed in the flow fluctuations are then reasonably independent of it and in this sense, they carry a degree of universality. Most importantly, in this regime, the three-dimensionality observed is intrinsic, and not induced by the forcing.

These results give a good idea of the conditions in which three-dimensionality is to be expected and how it arises. Since no measurements in the bulk were available, the question of how the appearance of three-dimensionality relates to that of the transversal component of velocity was left aside in this particular paper. Its link to weak three-dimensionality was investigated elsewhere in MHD and non-MHD flows (Poth erat (2012); Poth erat *et al.* (2013)). The question that now remains concerns how the different forms of three-dimensionality identified affect the flow dynamics. The scaling laws found in sections 2 and 5 show their impact on the intensity of both the average flow and its fluctuations. How they affect the finer properties of turbulence and in particular the

direction of the energy cascade still remains an open question.

The authors gratefully acknowledge financial support from the Deutsche Forschungsgemeinschaft (grant PO1210/4-1).

References

- AKKERMANS, R. A. D, KAMP, L. P. J., CLERCX, H. J. H & VAN HEIJST, G. H. F 2008 Intrinsic three-dimensionality in electromagnetically driven shallow flows. *EPL (Europhys. Lett.)* **83** (2), 24001.
- ALBOUSSIERE, T., USPENSKI, V. & MOREAU, R. 1999 Quasi-2d mhd turbulent shear layers. *Experimental Thermal and Fluid Science* **20** (20), 19–24.
- ALPHER, R. A., HURWITZ, H., JOHNSON, R. H. & WHITE, D. R. 1960 Some studies of free-surface mercury magnetohydrodynamics. *Rev. Mod. Phys* **4** (32), 758–774.
- ANDREEV, O., KOLESNIKOV, Y. & TCESS, A. 2013 Visualization of the ludford column. *J. Fluid Mech.* **721**, 438–453.
- BOECK, T., KRASNOV, D. & TCESS, A. 2008 Large-scale intermittency of liquid-metal channel flow in a magnetic field (101), 244501.
- CLERCX, H. J. H & VAN HEIJST, G 2009 Two-dimensional navier-stokes turbulence in bounded domains. *Appl. Mech. Rev.* **62**, 1–25.
- DAVIDSON, P. & POTH ERAT, A. 2002 A note on bodew adt-hartmann layer. *Eur. J. Mech. /B Fluids* **21** (5), 541–559.
- DOUSSET, V. & POTH ERAT, A 2012 Characterisation of the flow around a truncated cylinder in a duct in a spanwise magnetic field **691**, 341–367.
- DURAN-MATUTE, M., R. R. TRIELING, R. R. & VAN HEIJST, G. J. F. 2010 Scaling and asymmetry in an electromagnetically forced dipolar flow structure. *Phys. Rev. E* **83**, 016306.
- GREENSPAN, H. P. 1969 *Theory of Rotating Fluids*, The. Cambridge University Press.
- HUNT, J. C. R, LUDFORD, G. S. S. & HUNT, J. C. R 1968 Three dimensional mhd duct flow with strong transverse magnetic field. part 1 : Obstacles in a constant area duct. *J. Fluid Mech.* **33**, 693.
- KANARIS, N., ALBETS, X., GRIGORIADIS, D. & KASSINOS, K. 2013 3-d numerical simulations of mhd flow around a confined circular cylinder under low, moderate and strong magnetic fields. *Phys. Fluids* .
- KLEIN, R. & POTH ERAT, A. 2010 Appearance of three-dimensionality in wall bouded mhd flows. *Phys. Rev. Lett.* **104** (3).
- KLEIN, R., POTH ERAT, A. & ALFERJONOK, A. 2009 Experiment on a confined electrically driven vortex pair. *Phys. Rev. E* **79** (1), 016304 (14 pages).
- KLJUKIN, A. & TCESS, A. 1998 Direct measurement of the stream-function in a quasi-two-dimensional liquid metal flow. *Exp. Fluids* (25), 298–304.
- KOLMOGOROV, A. N. 1941 Local structure of turbulence in an incompressible fluid at very high reynolds numbers. *Dokl. Akad. Nauk. SSSR* **30**, 299–303.
- KRAICHMAN, R. H. 1967 Inertial ranges in two-dimensional turbulence. *Phys. Fluids* **10**, 1417.
- KRAICHMAN, R. H. 1971 Inertial ranges transfert in two- and three-dimensional turbulence. *J. Fluid Mech.* **47**, 525–535.
- LUDFORD, G. S. S. 1961 Effect of a very strong magnetic crossfield on steady motion through a slightly conducting fluid, the. *J. Fluid Mech.* **10**, 141–155.
- MOFFATT, H. K. 1967 On the suppression of turbulence by a uniform magnetic field. *J. Fluid Mech.* **28**, 571–592.
- MOREAU, R. 1990 *Magnetohydrodynamics*. Kluwer Academic Publisher.

- M UCK, B., G UNTER, C. & B UHLER, L. 2000 Buoyant three-dimensional mhd flows in rectangular ducts with internal obstacles. *J. Fluid Mech.* **418**, 265–295.
- PARET J., MARTEAU D., PAIREAU O. & P., TABELING 1997 Are flows electromagnetically forced in thin stratified layers two dimensional? *Phys. Fluids* **9** (10), 3102–3104.
- POTH ERAT, A. 2012 Three-dimensionality in quasi-two dimensional flows: Recirculations and "barrel" effets. *Europhys. Lett.* **98** (5).
- POTH ERAT, A. & DYMKO, V. 2010 Dns of low-rm mhd turbulence based on the least dissipative modes. *J. Fluid Mech.* **655**, 174–197.
- POTH ERAT, A, RUBICONI, F, CHARLES, Y. & DOUSSET, V 2013 Direct and inverse pumping in flows with homogenous and non-homogenous swirl. *EPJ E* p. submitted.
- POTH ERAT, A., SOMMERIA, J. & MOREAU, R. 2000 An effective two-dimensional model for mhd flows with transverse magnetic field. *J. Fluid Mech.* **424**, 75–100.
- POTH ERAT, A., SOMMERIA, J. & MOREAU, R. 2005 Numerical simulations of an effective two-dimensional model for flows with a transverse magnetic field. *J. Fluid Mech.* **534**, 115–143.
- ROBERTS, P. H. 1967 *Introduction to Magnetohydrodynamics*. Longmans.
- SCHMID, P. J. & HENNINGSON, D. S. 2001 *Stability and Transition in Shear Flows*. Springer-Verlag New York.
- SCHUMANN, U. 1976 Numerical simulation of the transition from three- to two-dimensional turbulence under a uniform magnetic field. *J. Fluid Mech.* **35**, 31–58.
- SHEBALIN, J. V., MATTHAEUS, W. H. & MONTGOMERY, D. 1983 Anisotropy in mhd turbulence due to a mean magnetic field. *J. Plasma Phys.* **29** (3), 525–547.
- SOMMERIA, J. 1986 Experimental study of the two-dimensional inverse energy cascade in a square box. *J. Fluid Mech.* **170**, 139–168.
- SOMMERIA, J. 1988 Electrically driven vortices in a strong magnetic field. *J. Fluid Mech.* **189**, 553–569.
- SOMMERIA, J. & MOREAU, R. 1982 Why, how and when mhd turbulence becomes two-dimensional. *J. Fluid Mech.* **118**, 507–518.
- SREENIVASAN, B. & ALBOUSSI ERE, T. 2002 Experimental study of a vortex in a magnetic field. *J. Fluid Mech.* **464**, 287–309.
- TABELING, PATRICK 2002 Two-dimensional turbulence: a physicist approach. *Phys. Rep.* (362), 1–62.
- THESS, A. & ZIKANOV, O. 2007 Transition from two-dimensional to three-dimensional magnetohydrodynamic turbulence. *J. Fluid Mech.* **579**, 383–412.
- TOSCHI, L. BIFERALE, MUSACCHIO, S. & F. 2012 Inverse energy cascade in three-dimensional isotropic turbulence. *Phys. Rev. Lett.* **108** (16), 164501.
- ZIKANOV, O. & THESS, A. 1998 Direct simulation of forced mhd turbulence at low magnetic reynolds number. *J. Fluid Mech.* **358**, 299–333.